International Journal of Solids and Structures 200–201 (2020) 213–230

Contents lists available at ScienceDirect

International Journal of Solids and Structures

journal homepage: www.elsevier.com/locate/ijsolstr

Finite element modeling of fiber reinforced cement composites using strong discontinuity approach with explicit representation of fibers

Ulrich Häussler-Combe *, Alaleh Shehni, Ahmad Chihadeh

Institute for Concrete Structures, Technische Universität Dresden, D-01062 Dresden, Germany

ARTICLE INFO

Article history:
Received 14 November 2019
Received in revised form 27 April 2020
Accepted 28 April 2020
Available online 24 May 2020

Keywords:
Fiber reinforced cement composites (FRCC)
Mesoscopic simulation
Strong discontinuity approach (SDA)
Random fiber orientation
Fiber-matrix interaction

ABSTRACT

Concrete is a predominant construction material due to a number of advantages. Disadvantages are given by its limited tensile strength and brittle tensile failure behavior. Fiber reinforced cement composites (FRCC) can improve these weaknesses to a large degree. But a proper composition design especially with respect to fiber and bond properties still follows a trial and error approach. Suitable simulation models can overcome this state whereby a mesoscopic view is chosen for the following. The Finite-Element-Method offers appropriate options due to its high flexibility. But special features are required which exceed standard FEM. This concerns modeling of crack formation in the cement matrix, a large number of fibers with arbitrary random distribution and the interaction of fibers with the cement matrix via bond. The paper addresses these items with (1) a further development of the Strong Discontinuity Approach to model discrete cracking of continuum elements on the element level, (2) discretization of single fibers by truss elements with truss nodes independently placed of continuum nodes, (3) connecting them by special bond elements. This allows for nonlinear behavior with respect to cement matrix, fiber material and bond laws. The contribution addresses theoretical basics, special implementation issues, a validation with simple configurations and a simulation of an FRCC experiment.

© 2020 Elsevier Ltd. All rights reserved.

1. Introduction

Strain–hardening cement-based composites (SHCC) are a special class of fiber reinforced cement composites (FRCC) which offers a high potential to improve structural behavior regarding tensile strength and ductility (Li et al., 1992; Li, 2003; Naaman, 2018). This is usually reached through a high number of thin, short polymer fibers mixed with a matrix of fine grained concrete. The modelled composite is a high-strength SHCC made with ultra-high molecular weight polyethylene (UHMWPE or shortly PE). They have a length of 6–10 mm and a diameter of 20 μm (Curosu et al., 2017). Nominal strength is 2 500 N/mm^2 with a brittle failure mode. Fibers are mixed up to 2% of volume with the cement matrix. For a proper interaction with the hydrophobic PE fibers the matrix in these composites has to provide a high packing density and strength (Curosu et al., 2017; Curosu et al., 2016). The matrix generally has a high cement content, a low water-to-binder ratio, small amount of fine sand and no coarse sand or aggregates. The mechanical response of FRCC is highly sensitive with respect to the cement matrix, the mechanical properties of the interface between the cement matrix and individual fibers, shape and the distribution of fibers in the composite (Bentur et al., 2007). A low tensile strength and fracture energy are beneficial regarding the formation of multiple steady state cracks and strain–hardening in the FRCC composite. The strength of bond between fibers and matrix should be moderated to let the fibers play their role in crack bridging while ensuring adequate free length for fiber deformation with crack opening and avoiding premature fiber failure.

The given ranges of properties of fibers and cement matrix allow for a wide range of properties of the composite material. This leads to challenges regarding material design. The composition of constituents still follows an experimental trial and error process when objectives for a composite material properties are given. Even with known characteristics of fibers and cement matrix their interaction due to bond, random fiber orientation and matrix cracking is complex and the behavior of the composite is generally not predictable with ordinary material models. Thus, a number of material models explicitly regarding fibers, cement matrix and bond have been developed. A respective mesoscopic scale treats a composite as a structure and put complex composite material behavior down to a structural behavior of constituents with known

* Corresponding author.
E-mail addresses: ulrich.haeussler-combe@tu-dresden.de (U. Häussler-Combe), alaleh.shehni@tu-dresden.de (A. Shehni), ahmad.chihadeh@tu-dresden.de (A. Chihadeh).

https://doi.org/10.1016/j.ijsolstr.2020.04.036
0020-7683/© 2020 Elsevier Ltd. All rights reserved.

behavior of each. The Finite-Element-Method (FEM) has proven to provide an extremely high adaptability to model all types of structures (Bathe, 1996; Belytschko et al., 2000). Compared to standard finite elements specific features are discussed in the current paper regarding mesoscopic modeling of FRCC. This concerns crack formation in the cement matrix, a large number of fibers with arbitrary random distribution and the interaction of fibers with cement matrix via bond.

Smeared crack or discrete crack approaches are basic alternatives to model cracking. The former need regularization techniques (Bažant et al., 1983; Bažant et al., 1988; Jirásek, 1998; Pamin and de Borst, 1999), to reach mesh objectivity and to reproduce crack energies. Such techniques become practically intricate in case of element sizes much larger or smaller compared to the thickness of so called crack bands developing due to the quasi-brittle behavior of concrete. Discrete cracks can be modeled by using interface elements located along continuum elements boundaries (López et al., 2008), however, this approach requires remeshing technique to capture crack paths (Bouchard et al., 2000). To avoid using interface elements with the need for remeshing, discrete cracks can be modeled by using two other approaches: Extended-Finite-Element (XFEM) (Moës et al., 1999; Fries et al., 2010; Stolarska et al., 2001) and the Strong-Discontinuity-Approach (SDA) (Dvorkin et al., 1990; Jirásek, 2000; Oliver et al., 2003; Alfaiate et al., 2003; Alfaiate and Sluys, 2007). Both allow for an explicit evaluation of crack width to imply crack tractions and need no further regularization for mesh objectivity and fracture energy reproduction. XFEM introduces additional degrees of freedom on the system level which makes this approach inconvenient for structures with a large number of cracks. SDA condenses discontinuity degrees of freedom on the element level leading to enhanced element formulations which do not explicitly carry additional degrees of freedom to the system level. This makes SDA more appropriate in case of a large number of cracks.

So far three different classes are used in the formulation of SDA: Statically Optimal Symmetric (SOS), Kinematically Optimal Symmetric (KOS), and Statically and Kinematically Optimal Nonsymmetric (SKON) (Jirásek, 2000; Zhang et al., 2015). The SDA formulation used in this paper is similar to the KOS, both follow the same way in constructing the matrix of the strain functions in the discontinuity. The above mentioned classes have the Hu-Washizu principle as a basis for the development of the formulation, see Appendix A.

Regarding the discontinuity or the crack path across neighboring elements two alternatives have been introduced: continuous path and discontinuous path. Crack path continuity may be enforced by tracking algorithms (Oliver et al., 2004) but this stimulates locking effects, specifically in the SOS formulation (Zhang et al., 2015). The extension of crack path discontinuities can generally be reduced by reducing element sizes whereby the crack path is clearly indicated. A control of implausible multiple crack path courses is proposed with adaption methods (Sancho et al., 2007). Relations for crack tractions depending on crack width are basically derived from experimental investigations about concrete tensile failure behavior (Sancho et al., 2007; Costa et al., 2009; Kim, 2013). They generally introduce nonlinearities, e.g., in case nonmonotonic behavior with un- and reloading of cracks in inhomogeneous structures during a loading history. The modeling of such phenomena is not trivial but is not explicitly addressed in the current literature as far as can be seen.

Fibers have to be regarded in addition to the cracked continuum for modeling of FRCC. Based on studies discussed in (Kunieda et al., 2011; Smolcic and Ozbolt, 2017) such models are generally based on: (1) FEM using a smeared crack approach and stress–strain curves obtained from experiments (Han et al., 2003; Suwada et al., 2006). These models are restricted to be used only for specific structural elements under the same conditions as applied for experimental specimen (Padmarajaiah and Ramaswamy, 2002). (2) Discrete crack approaches with crack width determination as discussed above which is utilized with respect to advanced mechanical property determination due to fiber bridging (Fischer et al., 2007; Maalej, 2001). (3) Bond stress-slip based models where the fibers are discretely modeled in the cement matrix at the meso-level (Bolander and Saito, 1997). In this approach, a wide range of FRCC regardless of fiber lengths and fiber types can be analyzed. Discrete or smeared approaches can be applied depending on the crack traction-crack width law or stress-strain softening law whereby the material properties are assumed as homogenized finally yielding a macroscopic approach suitable for the analysis of whole structures. Mesoscopic models explicitly distinguishing cement matrix, fibers and fiber-matrix bond are summarized by (Bitencourt et al., 2019). Fibers are treated as embedded elements whereas the mesh of a fiber cloud is generated independently from mesh of cement matrix and a coupling procedure is used to connect these two independent meshes. These models are also able to investigate the effect of production techniques and conditions as well (Švec et al., 2014). Some proposals modify the constitutive law to consider the effect of fiber–matrix interaction whereas bond is considered as rigid (Pros et al., 2012; Cunha et al., 2011; Cunha et al., 2012). Fibers are also modeled as embedded elements such that the effect of them is considered by discrete forces which are applied to the continuum mesh near the fiber ends position (Radtke et al., 2011). Furthermore, the effect of fibers is described using closing loads as a replacement for the interaction between a fiber, crossing a cohesive crack and the matrix (Ruiz, 2001). Various approaches for the fiber–matrix interaction use analytical relations derived from pullout tests, e.g. (Laranjeira, 2010) basing on experimental investigations (Laranjeira et al., 2010; Laranjeira et al., 2010), or (Radtke et al., 2011) concluding from the model by (Hartig et al., 2008). Lattice models as alternatives to FEM are proposed, e.g., by (Kang and Bolander, 2017).

The current paper uses the mesoscopic approach combining models for discrete matrix cracking, explicit fibers and flexible bond for each single fiber in a consistent and straightforward manner. It is organized as follows: The following section describes model discretization by finite elements whereby small displacements and strains are assumed. The discretized model differentiates continuous and discontinuous contributions to the displacement field of the cement matrix continuum whereby the discontinuous contributions are treated on the element level with SDA. Discontinuous displacement contributions are also synonymously referred to as cracks in the following. The extension of an uncracked continuum element to a cracked SDA element is ruled by criteria to be defined and depends on the loading history. This includes the possibility for multiple cracking of a single element in different orientations. Cracking is combined with crack tractions transferred over cracks within the fictitious or cohesive crack concept to cover fracture energy. This is introduced for monotonic crack loading, unloading, crack closure and reloading. Furthermore, truss elements with their own nodes independent from continuum element nodes are arbitrarily embedded in the continuum to model single fibers. The interaction between continuum elements and single truss elements is ruled by special bond elements connecting truss nodes and neighbored continuum nodes, for both uncracked and cracked elements in the same way whereby nonlinear bond laws may be used.

The model is validated in the third section with investigations on a cracked one-element setup, a single fiber embedded in surrounding continuum elements whereby including the calibration of bond laws and finally the simulation of an experimental specimen of FRCC. In contrast to examples given in above mentioned references the FRCC simulation shows a large number of crack

paths due to interaction of the cement matrix with fibers. The paper closes with some conclusions and potential developments.

2. Simulation model

2.1. Continuum modeling with finite elements

Structural analysis bases upon equilibrium, material laws and kinematic assumptions. This is shortly summarized with respect to the Finite Element Method (FEM) for later reference. The displacement field is assumed to consist of a continuous part $\bar{\boldsymbol{u}}$ and an enhancing part $\hat{\boldsymbol{u}}$ which might include discontinuous contributions

$$\boldsymbol{u}(\boldsymbol{x}) = \bar{\boldsymbol{u}}(\boldsymbol{x}) + \hat{\boldsymbol{u}}(\boldsymbol{x}) \tag{1}$$

with a local coordinate $\boldsymbol{x}$. This corresponds to a KOS approach. Regarding standard FEM the discretization of the continuous displacement contribution is performed with

$$\bar{\boldsymbol{u}}(\boldsymbol{x}) = \boldsymbol{N}(\boldsymbol{x}) \cdot \bar{\boldsymbol{u}}_I \tag{2}$$

with a matrix of shape functions $\boldsymbol{N}$ and a vector of nodal displacements $\bar{\boldsymbol{u}}_I$. This leads to strains

$$\boldsymbol{\epsilon}(\boldsymbol{x}) = \frac{\partial \bar{\boldsymbol{u}}}{\partial \boldsymbol{x}} = \boldsymbol{B}(\boldsymbol{x}) \cdot \bar{\boldsymbol{u}}_I \tag{3}$$

with the matrix of shape function derivatives $\boldsymbol{B}$ (Bathe, 1996). The equilibrium condition is formulated in the weak form

$$\int_V \delta\boldsymbol{\epsilon}^T \cdot \boldsymbol{\sigma}\, \mathrm{d}V = \int_V \delta\bar{\boldsymbol{u}}^T \cdot \boldsymbol{b}\, \mathrm{d}V + \int_{A_t} \delta\bar{\boldsymbol{u}}^T \cdot \boldsymbol{t}\, \mathrm{d}A \tag{4}$$

with virtual displacements $\delta\bar{\boldsymbol{u}}$ and derived virtual strains $\delta\boldsymbol{\epsilon}$, stresses $\boldsymbol{\sigma}$, body forces $\boldsymbol{b}$, the domain under consideration V and its boundary A_t with prescribed tractions $\boldsymbol{t}$ under the condition that nodal displacements fulfill the displacement boundary conditions, compare also Eq. (A.3)$_1$ with a derivation in a general context. With a continuous field $\bar{\boldsymbol{u}}$ this can be applied to a whole domain of a structure or also to subdomains of it, e.g. domains of single finite elements.

Finally, a material law is given by connecting stresses to strains which in a general form is described with

$$\boldsymbol{\sigma} = \boldsymbol{\sigma}(\boldsymbol{\epsilon}) \tag{5}$$

or in an incremental form

$$\dot{\boldsymbol{\sigma}} = \boldsymbol{C}_T(\boldsymbol{\epsilon}) \cdot \dot{\boldsymbol{\epsilon}} \tag{6}$$

with time derivatives $\dot{\boldsymbol{\sigma}}, \dot{\boldsymbol{\epsilon}}$ of stress and strain with respect to a loading time t and a tangential material stiffness $\boldsymbol{C}_T$. Using Eqs. (2, 3) with Eq. (4) leads to the discretized equilibrium conditions

$$\delta\bar{\boldsymbol{u}}^T \cdot (\boldsymbol{p}_I - \boldsymbol{f}_I) = 0 \tag{7}$$

with internal nodal forces

$$\boldsymbol{f}_I = \int_V \boldsymbol{B}^T \cdot \boldsymbol{\sigma}\, \mathrm{d}V \tag{8}$$

and external nodal forces

$$\boldsymbol{p}_I = \int_V \boldsymbol{N}^T \cdot \boldsymbol{b}\, \mathrm{d}V + \int_{A_t} \boldsymbol{N}^T \cdot \boldsymbol{t}\, \mathrm{d}A \tag{9}$$

Virtual displacements $\delta\bar{\boldsymbol{u}}$ are kept in this formulation for a later combination with the equilibrium condition covering a discontinuous displacement field. A linearization is performed with

$$\dot{\boldsymbol{f}}_I = \int_V \boldsymbol{B}^T \cdot \dot{\boldsymbol{\sigma}}\, \mathrm{d}V = \int_V \boldsymbol{B}^T \cdot \boldsymbol{C}_T \cdot \boldsymbol{B}\, \mathrm{d}V \cdot \dot{\bar{\boldsymbol{u}}}_I = \boldsymbol{K}_T \cdot \dot{\bar{\boldsymbol{u}}}_I \tag{10}$$

with the tangential stiffness matrix $\boldsymbol{K}_T$.

2.2. Explicit crack modeling with SDA

The following discussion to a large extent follows (Alfaiate et al., 2003) whereby adding some aspects. A displacement discontinuity is regarded on the element level. To begin with, the following refers to a 2D continuum element with four nodes with a single discontinuity, see Fig. 1. Rules for kinematics, equilibrium and material behviour are again utilized within this setup. Regarding kinematics the total displacement is decomposed according to Eq. (1) with an enhanced discontinuous part

$$\hat{\boldsymbol{u}}(\boldsymbol{x}) = \mathcal{H}\, \|\boldsymbol{u}(\boldsymbol{x})\| \tag{11}$$

composed of a discontinuity splitting term

$$\mathcal{H} = \begin{cases} r, & \boldsymbol{x} \in V^+ \\ r-1, & else \end{cases} \tag{12}$$

with a constant splitting parameter $0 \leqslant r \leqslant 1$ to be chosen and a rigid body displacement term

$$\|\boldsymbol{u}(\boldsymbol{x})\| = \begin{bmatrix} 1 & 0 & -y+y_0 \\ 0 & 1 & x-x_0 \end{bmatrix} \cdot \begin{pmatrix} u_{0,x} \\ u_{0,y} \\ \beta \end{pmatrix} = \boldsymbol{N}_w(\boldsymbol{x}) \cdot \boldsymbol{w} \tag{13}$$

with translational degrees of freedom $u_{0,x}, u_{0,y}$ and a rotational degree of freedom β. A value $r = 0.5$ is generally used in the following. The discontinuity degrees of freedom collected in $\boldsymbol{w}$ in connection with the discontinuity shape function $\boldsymbol{N}_w$ lead to a wedged crack with center $\boldsymbol{x}_0$ whereby the crack orientation is ruled by the element's splitting into domains V^-, V^+. Eq. (13) leads to a rigid body displacement of nodes

$$\hat{\boldsymbol{u}}_I = \begin{bmatrix} \boldsymbol{N}_w(\boldsymbol{x}_1) \\ \boldsymbol{N}_w(\boldsymbol{x}_2) \\ \boldsymbol{N}_w(\boldsymbol{x}_3) \\ \boldsymbol{N}_w(\boldsymbol{x}_4) \end{bmatrix} \cdot \boldsymbol{w} = \boldsymbol{M}_w \cdot \boldsymbol{w} \tag{14}$$

with nodal coordinates $\boldsymbol{x}_I$, $I = 1 \ldots 4$. This is split into domains V^+, V^- by $\boldsymbol{\mathcal{H}} \cdot \hat{\boldsymbol{u}}_I$ with a diagonal

$$\boldsymbol{\mathcal{H}} = \begin{bmatrix} \mathcal{H}_1 & & & & \\ & \mathcal{H}_1 & & & \\ & & \ddots & & \\ & & & \mathcal{H}_4 & \\ & & & & \mathcal{H}_4 \end{bmatrix} \tag{15}$$

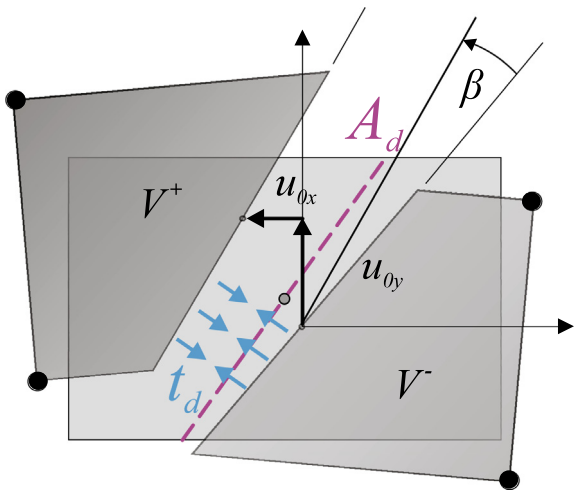


Fig. 1. Kinematics of strong discontinuity approach.

with $\mathcal{H}_I$ from Eq. (12) according to nodal mappings into V^+ or V^-, see Fig. 1.

Nodal displacements $\bar{\boldsymbol{u}}_I$ defining the continuous displacement field, see Eq. (2), and nodal displacements $\mathcal{H}\cdot\hat{\boldsymbol{u}}_I$ defining the discontinuous displacement field together form the nodal displacements for the total displacement

$$\boldsymbol{u}_I = \bar{\boldsymbol{u}}_I + \mathcal{H}\cdot\hat{\boldsymbol{u}}_I \tag{16}$$

The interpolation of the total displacement field is determined with

$$\boldsymbol{u}(\boldsymbol{x}) = \boldsymbol{N}(\boldsymbol{x})\cdot\boldsymbol{u}_I = \boldsymbol{N}(\boldsymbol{x})\cdot\bar{\boldsymbol{u}}_I + \boldsymbol{N}(\boldsymbol{x})\cdot\mathcal{H}\cdot\hat{\boldsymbol{u}}_I \tag{17}$$

i.e., the interpolation operator is applied after superposing continuous and enhanced nodal contributions which is characteristic for KOS (Jirásek, 2000) and includes a continuous mapping of the discontinuous displacement field. With total nodal displacements $\boldsymbol{u}$ given from a computation on the system level and the discontinuity degrees of freedom $\boldsymbol{w}$ determined on element level, see following Section 2.4, the actual continuous field $\bar{\boldsymbol{u}}$ is recovered with

$$\bar{\boldsymbol{u}}(\boldsymbol{x}) = \boldsymbol{N}(\boldsymbol{x})\cdot\boldsymbol{u}_I - \boldsymbol{N}(\boldsymbol{x})\cdot\mathcal{H}\cdot\boldsymbol{M}_w\cdot\boldsymbol{w} \tag{18}$$

using Eqs. (17, 14). Continuum strains are derived from the actual continuous field with

$$\boldsymbol{\epsilon} = \frac{\partial\bar{\boldsymbol{u}}}{\partial\boldsymbol{x}} = \boldsymbol{B}(\boldsymbol{x})\cdot\boldsymbol{u}_I - \boldsymbol{B}_w(\boldsymbol{x})\cdot\boldsymbol{w} \tag{19}$$

with $\boldsymbol{B}$ according to Eq. (3) and

$$\boldsymbol{B}_w(\boldsymbol{x}) = \boldsymbol{B}(\boldsymbol{x})\cdot\mathcal{H}\cdot\boldsymbol{M}_w \tag{20}$$

This leads to zero strains in case $\boldsymbol{u}_I = \mathcal{H}\cdot\hat{\boldsymbol{u}}_I$, i.e. when the total nodal displacements reproduce the discontinuous displacement field $\mathcal{H}\,\|\boldsymbol{u}(\boldsymbol{x})\|$.

The approach may be extended to multiple fields of displacement discontinuities. A secondary discontinuity, e.g., is introduced with the extension of Eq. (11)

$$\begin{aligned}\boldsymbol{u}(\boldsymbol{x}) &= \bar{\boldsymbol{u}}(\boldsymbol{x}) + \mathcal{H}_1\,\|\boldsymbol{u}(\boldsymbol{x})\|_1 + \mathcal{H}_2\,\|\boldsymbol{u}(\boldsymbol{x})\|_2\\ &= \bar{\boldsymbol{u}}(\boldsymbol{x}) + \mathcal{H}_1\boldsymbol{N}_{w,1}\cdot\boldsymbol{w}_1 + \mathcal{H}_2\boldsymbol{N}_{w,2}\cdot\boldsymbol{w}_2\\ &= \bar{\boldsymbol{u}}(\boldsymbol{x}) + [\,\mathcal{H}_1\boldsymbol{N}_{w1}\quad\mathcal{H}_2\boldsymbol{N}_{w,2}\,]\cdot\begin{pmatrix}\boldsymbol{w}_1\\ \boldsymbol{w}_2\end{pmatrix}\\ &= \bar{\boldsymbol{u}}(\boldsymbol{x}) + \boldsymbol{N}_w^{II}\cdot\boldsymbol{w}^{II}\end{aligned} \tag{21}$$

The extensions to $\boldsymbol{M}_w^{II}$, see Eq. (14), and $\boldsymbol{B}_w^{II}$, see Eq. (20), are straightforward with the number of discontinuity degrees of freedom doubled on the element level whereby $\mathcal{H}$ remains unchanged. The application of SDA to other than four-node 2D elements, in particular triangular elements, and 3D elements is also straightforward. The latter introduces six discontinuity degrees of freedom for each discontinuity according to spatial rigid body movements and has a plane convex polygon separating an element. Furthermore, regarding rotating crack concepts a discontinuity contour may basically be changed with modifications of $\mathcal{H}$ during a loading history.

The discussion has treated kinematics so far. Discontinuity equilibrium has to be formulated in the next step. A weak form

$$\begin{aligned}&\int_V \mathcal{H}\,\delta\nabla^{sym}\|\boldsymbol{u}\|^T\cdot\boldsymbol{\sigma}\,\mathrm{d}V + \int_{A_d}\delta\|\boldsymbol{u}\|^T\cdot\boldsymbol{t}_d\,\mathrm{d}A\\ &= \int_V \mathcal{H}\,\delta\|\boldsymbol{u}\|^T\cdot\boldsymbol{b}\,\mathrm{d}V + \int_{A_t}\mathcal{H}\,\delta\|\boldsymbol{u}\|^T\cdot\boldsymbol{t}\,\mathrm{d}A\end{aligned} \tag{22}$$

in analogy to Eq. (4) is used with the symmetric Nabla operator ∇^{sym}, the path A_d along the discontinuity and the traction t_d along the discontinuity, see Fig. 1 and compare also Eq. (A.21) with a derivation in a general context. The discontinuity interpolation Eq. (13) yields

$$\begin{aligned}\nabla^{sym}\|\boldsymbol{u}\| &= 0\\ \delta\|\boldsymbol{u}\| &= \boldsymbol{N}_w\cdot\delta\boldsymbol{w}\end{aligned} \tag{23}$$

which in analogy to Eq. (7) leads to a discretized discontinuity equilibrium

$$\delta\boldsymbol{w}^T\cdot(\boldsymbol{p}_w - \boldsymbol{f}_w) = 0 \tag{24}$$

with

$$\boldsymbol{f}_w = \int_{A_d}\boldsymbol{N}_w^T\cdot\boldsymbol{t}_d\,\mathrm{d}A \tag{25}$$

and

$$\boldsymbol{p}_w = \int_V \mathcal{H}\boldsymbol{N}_w^T\cdot\boldsymbol{b}\,\mathrm{d}V + \int_{A_t}\mathcal{H}\boldsymbol{N}_w^T\cdot\boldsymbol{t}\,\mathrm{d}A \tag{26}$$

In contrast to Eqs. (8) and (9) $\boldsymbol{f}_w, \boldsymbol{p}_w$ are not nodal forces assigned to nodal degrees of freedom but generalized 'discontinuity' forces assigned to the discontinuity degrees of freedom whereby $\boldsymbol{f}_w$ can be considered as internal due its dependence on generalized internal 'stresses' $\boldsymbol{t}_d$ and $\boldsymbol{p}_w$ as external due to its dependence on given loading terms $\boldsymbol{b}, \boldsymbol{t}$.

Finally, a generalized type of material behavior has to be regarded. In analogy to Eq. (5) a general form is given by

$$\boldsymbol{t}_d = \boldsymbol{t}_d(\boldsymbol{w}) \tag{27}$$

which follows the fictitious or cohesive crack model (Hillerborg et al., 1976). In analogy to Eq. (6) it should be specified in an incremental form

$$\dot{\boldsymbol{t}}_d = \boldsymbol{C}_{Tw}(\boldsymbol{w})\cdot\dot{\boldsymbol{w}} \tag{28}$$

This allows for a linearization of the internal discontinuity forces

$$\dot{\boldsymbol{f}}_w = \int_{A_d}\boldsymbol{N}_w^T\cdot\boldsymbol{C}_{Tw}\cdot\boldsymbol{N}_w\,\mathrm{d}A\cdot\dot{\boldsymbol{w}} = \boldsymbol{K}_{T,nn}\cdot\dot{\boldsymbol{w}} \tag{29}$$

with a tangential discontinuity stiffness matrix $\boldsymbol{K}_{T,nn}$ in analogy to Eq. (10).

2.3. Coupling of continuum to discontinuity

The discretized continuous part described by Eq. (7) and the part including a discontinuity only described by Eq. (24) have to be coupled. This is started by deriving the virtual continuous displacement from the total displacement and the discontinuous part as given with Eqs. (1, 11)

$$\delta\bar{\boldsymbol{u}} = \delta\boldsymbol{u} - \mathcal{H}\,\delta\|\boldsymbol{u}\| \tag{30}$$

and applying the interpolations Eqs. (17, 13)

$$\delta\bar{\boldsymbol{u}} = \boldsymbol{N}\cdot\delta\boldsymbol{u}_I - \mathcal{H}\boldsymbol{N}_w\cdot\delta\boldsymbol{w} \tag{31}$$

Furthermore, virtual strains are given by Eq. (19)

$$\delta\boldsymbol{\epsilon} = \boldsymbol{B}(\boldsymbol{x})\cdot\delta\boldsymbol{u}_I - \boldsymbol{B}_w(\boldsymbol{x})\cdot\delta\boldsymbol{w} \tag{32}$$

Eq. (4) is still applicable due to continuity of $\bar{\boldsymbol{u}}$ and $\delta\bar{\boldsymbol{u}}$. Thus the application to the weak equilibrium form for the continuous field Eq. (4)

$$\begin{aligned}&\delta\boldsymbol{u}_I^T\cdot\int_V\boldsymbol{B}^T\cdot\boldsymbol{\sigma}\,\mathrm{d}V - \delta\boldsymbol{w}^T\cdot\int_V\boldsymbol{B}_w^T\cdot\boldsymbol{\sigma}\,\mathrm{d}V\\ &\quad= \delta\boldsymbol{u}_I^T\cdot\int_V\boldsymbol{N}^T\cdot\boldsymbol{b}\,\mathrm{d}V - \delta\boldsymbol{w}^T\cdot\int_V\mathcal{H}\boldsymbol{N}_w^T\cdot\boldsymbol{b}\,\mathrm{d}V\\ &\qquad+ \delta\boldsymbol{u}_I^T\cdot\int_{A_t}\boldsymbol{N}^T\cdot\boldsymbol{t}\,\mathrm{d}A - \delta\boldsymbol{w}^T\cdot\int_{A_t}\mathcal{H}\boldsymbol{N}_w^T\cdot\boldsymbol{t}\,\mathrm{d}A\end{aligned} \tag{33}$$

leads to an extended form of Eq. (7)

$$\delta\boldsymbol{u}^T(\boldsymbol{p}_I - \boldsymbol{f}_I) - \delta\boldsymbol{w}^T\cdot(\boldsymbol{p}_w - \boldsymbol{f}_c) = 0 \tag{34}$$

with $\boldsymbol{p}_I$ from Eq. (9), $\boldsymbol{f}_I$ from Eq. (8), $\boldsymbol{p}_w$ from Eq. (26) and coupling discontinuity forces

$$\boldsymbol{f}_c = \int_V \boldsymbol{B}_w^T \cdot \boldsymbol{\sigma}\, \mathrm{d}V \tag{35}$$

with $\boldsymbol{B}_w$ from Eq. (20). Adding the conditions for the extended discretized equilibrium for the continuous field Eq. (34) and the discretized equilibrium for the discontinuous field Eq. (24) yields two sets of combined discretized equilibrium conditions for a particular element

$$\begin{aligned} \boldsymbol{r}_I &= \boldsymbol{p}_I - \boldsymbol{f}_I = 0 \\ \boldsymbol{r}_w &= \boldsymbol{f}_c - \boldsymbol{f}_w = 0 \end{aligned} \tag{36}$$

with residuals $\boldsymbol{r}_I, \boldsymbol{r}_w$ as $\delta\boldsymbol{u}_I, \delta\boldsymbol{w}$ are independent and arbitrary.

Terms of Eq. (36) remain to be linearized with their derivations with respect to the loading time t. The internal nodal forces time derivative $\dot{\boldsymbol{f}}_I$ from Eq. (10) has to be extended to imply the total displacement time derivative by Eq. (19)

$$\begin{aligned} \dot{\boldsymbol{f}}_I &= \int_V \boldsymbol{B}^T \cdot \dot{\boldsymbol{\sigma}}\, \mathrm{d}V = \int_V \boldsymbol{B}^T \cdot \boldsymbol{C}_T \cdot \dot{\boldsymbol{\epsilon}}\, \mathrm{d}V \\ &= \int_V \boldsymbol{B}^T \cdot \boldsymbol{C}_T \cdot \boldsymbol{B}\, \mathrm{d}V \cdot \dot{\boldsymbol{u}}_I - \int_V \boldsymbol{B}^T \cdot \boldsymbol{C}_T \cdot \boldsymbol{B}_w\, \mathrm{d}V \cdot \dot{\boldsymbol{w}} \\ &= \boldsymbol{K}_{T,uu} \cdot \dot{\boldsymbol{u}}_I - \boldsymbol{K}_{T,uw} \cdot \dot{\boldsymbol{w}} \end{aligned} \tag{37}$$

with the tangential stiffness matrices $\boldsymbol{K}_{T,uu}, \boldsymbol{K}_{T,uw}$. The time derivative of the coupling discontinuity forces, see Eq. (35), is derived in an analogous way

$$\begin{aligned} \dot{\boldsymbol{f}}_c &= \int_V \boldsymbol{B}_w^T \cdot \boldsymbol{C}_T \cdot \boldsymbol{B}\, \mathrm{d}V \cdot \dot{\boldsymbol{u}}_I - \int_V \boldsymbol{B}_w^T \cdot \boldsymbol{C}_T \cdot \boldsymbol{B}_w\, \mathrm{d}V \cdot \dot{\boldsymbol{w}} \\ &= \boldsymbol{K}_{T,wu} \cdot \dot{\boldsymbol{u}}_I - \boldsymbol{K}_{T,ww} \cdot \dot{\boldsymbol{w}} \end{aligned} \tag{38}$$

with further tangential stiffness matrices $\boldsymbol{K}_{T,wu}, \boldsymbol{K}_{T,ww}$. The time derivative of the internal discontinuity forces $\boldsymbol{f}_w$ is given by Eq. (29) and $\dot{\boldsymbol{p}}_I$, see Eq. (9), is ruled by prescribed $\dot{\boldsymbol{b}}, \dot{\boldsymbol{t}}$.

Thus, incremental equilibrium conditions $\dot{\boldsymbol{p}}_I - \dot{\boldsymbol{f}}_I = 0,\ \dot{\boldsymbol{f}}_c - \dot{\boldsymbol{f}}_w = 0$ corresponding to Eq. (36) are given with

$$\begin{bmatrix} \boldsymbol{K}_{T,uu} & -\boldsymbol{K}_{T,uw} \\ -\boldsymbol{K}_{T,wu} & \boldsymbol{K}_{T,ww} + \boldsymbol{K}_{Tnn} \end{bmatrix} \cdot \begin{pmatrix} \dot{\boldsymbol{u}}_I \\ \dot{\boldsymbol{w}} \end{pmatrix} = \begin{pmatrix} \dot{\boldsymbol{p}} \\ 0 \end{pmatrix} \tag{39}$$

This is decoupled with the second row to be solved firstly on the element level

$$\dot{\boldsymbol{w}} = \mathcal{D}_{T,w} \cdot \dot{\boldsymbol{u}}_I \tag{40}$$

with

$$\mathcal{D}_{T,w} = \left[\boldsymbol{K}_{T,ww} + \boldsymbol{K}_{Tnn}\right]^{-1} \cdot \boldsymbol{K}_{T,wu} \tag{41}$$

and the solution $\dot{\boldsymbol{w}}$ to be used for the first row

$$\mathcal{K}_{T,u} \cdot \dot{\boldsymbol{u}}_I = \dot{\boldsymbol{p}} \tag{42}$$

with

$$\mathcal{K}_{T,u} = \boldsymbol{K}_{T,uu} - \boldsymbol{K}_{T,uw} \cdot \left[\boldsymbol{K}_{T,ww} + \boldsymbol{K}_{Tnn}\right]^{-1} \cdot \boldsymbol{K}_{T,wu} \tag{43}$$

whereby the latter is assembled on the system level and solved for the nodal displacement increments of the whole system.

2.4. Loading time discretization and equilibrium iteration

The Euler backward approach with a constant time step $t^i = \Delta t \cdot i,\ i = 1 \ldots n$ is used for loading time discretization. It is performed with

$$\begin{aligned} \dot{\boldsymbol{w}}^i &\approx \frac{\Delta \boldsymbol{w}}{\Delta t} = \frac{\boldsymbol{w}^i - \boldsymbol{w}^{i-1}}{\Delta t} \\ \dot{\boldsymbol{u}}_I^i &\approx \frac{\Delta \boldsymbol{u}_I}{\Delta t} = \frac{\boldsymbol{u}_I^i - \boldsymbol{u}_I^{i-1}}{\Delta t} \\ \dot{\boldsymbol{p}}^i &\approx \frac{\Delta \boldsymbol{p}}{\Delta t} = \frac{\boldsymbol{p}^i - \boldsymbol{p}^{i-1}}{\Delta t} \end{aligned} \tag{44}$$

Equilibrium $\boldsymbol{p}_I^{i-1} - \boldsymbol{f}_I^{i-1} = 0,\ \boldsymbol{f}_c^{i-1} - \boldsymbol{f}_w^{i-1} = 0$ is assumed for the preceding time t^{i-1}. The loading $\boldsymbol{p}^i$ is basically prescribed for all time steps. This yields a nonlinear set of algebraic equations

$$\mathcal{K}_{T,u}(\boldsymbol{u}_I, \boldsymbol{w}) \cdot \Delta \boldsymbol{u}_I = \Delta \boldsymbol{p} \tag{45}$$

according to Eq. (42) to gain a solution $\boldsymbol{u}_I^i = \boldsymbol{u}_I^{i-1} + \Delta \boldsymbol{u}_I$ on the system level with a potential residuum

$$\boldsymbol{r}_I = \boldsymbol{p}_I - \boldsymbol{f}_I \tag{46}$$

see Eq. $(36)_1$. Iterated values of $\boldsymbol{u}_I^i, \Delta \boldsymbol{u}_I$ are indicated with ${}^{\nu}\boldsymbol{u}_I^i, \Delta^{\nu}\boldsymbol{u}_I$. A first starter for Eq. (45) is given with

$$\mathcal{K}_{T,u}\left(\boldsymbol{u}_I^{i-1}, \boldsymbol{w}^{i-1}\right) \cdot \delta^1 \boldsymbol{u}_I = \Delta \boldsymbol{p} \tag{47}$$

and $\Delta^1 \boldsymbol{u}_I = \delta^1 \boldsymbol{u}_I$ and ${}^1\boldsymbol{u}_I^i = \boldsymbol{u}_I^{i-1} + \Delta^1 \boldsymbol{u}$.

The displacements derived on the system level can be used for each element to iterate for its discontinuity degrees of freedom using the generally nonlinear set of equations

$$\Delta \boldsymbol{w} = \mathcal{D}_{T,w}(\boldsymbol{u}_I, \boldsymbol{w}) \cdot \Delta \boldsymbol{u}_I \tag{48}$$

according to Eq. (40) with a potential residuum

$$\boldsymbol{r}_w = \boldsymbol{f}_c - \boldsymbol{f}_w \tag{49}$$

see Eq. $(36)_2$. A first starter for Eq. (48) is given with

$$\delta^1 \boldsymbol{w} = \mathcal{D}_{T,w}\left({}^1\boldsymbol{u}_I^i, \boldsymbol{w}^{i-1}\right) \cdot \Delta^1 \boldsymbol{u}_I \tag{50}$$

and $\Delta^1 \boldsymbol{w} = \delta^1 \boldsymbol{w}$ and ${}^1\boldsymbol{w}^i = \boldsymbol{w}^{i-1} + \Delta^1 \boldsymbol{w}$ and a residuum

$${}^1\boldsymbol{r}_w = \boldsymbol{f}_c\left({}^1\boldsymbol{u}_I^i, {}^1\boldsymbol{w}^i\right) - \boldsymbol{f}_w\left({}^1\boldsymbol{w}^i\right) \tag{51}$$

For $|{}^1\boldsymbol{r}_w| > tol_w$ this is iteratively solved with the Newton–Raphson method in the general form

$$\begin{aligned} \delta^{\mu+1}\boldsymbol{w} &= -\left.\frac{\partial \boldsymbol{r}_w(\boldsymbol{w})}{\partial \boldsymbol{w}}\right|_{\boldsymbol{w}={}^{\mu}\boldsymbol{w}^i} \cdot {}^{\mu}\boldsymbol{r}_w \\ \Delta^{\mu+1}\boldsymbol{w} &= \Delta^{\mu}\boldsymbol{w} + \delta^{\mu+1}\boldsymbol{w} \\ {}^{\mu+1}\boldsymbol{w}^i &= \boldsymbol{w}^{i-1} + \Delta^{\mu+1}\boldsymbol{w} \end{aligned} \tag{52}$$

The Jacobian is given with

$$\frac{\partial \boldsymbol{r}_w(\boldsymbol{w})}{\partial \boldsymbol{w}} = \frac{\boldsymbol{f}_c\left({}^1\boldsymbol{u}_I^i, \boldsymbol{w}\right)}{\partial \boldsymbol{w}} - \frac{\boldsymbol{f}_w(\boldsymbol{w})}{\partial \boldsymbol{w}} = -\left(\boldsymbol{K}_{T,ww} + \boldsymbol{K}_{T,nn}\right) \tag{53}$$

see Eqs. (38) and (29).

With $|{}^{\mu}\boldsymbol{r}_w| \approx 0$ and discontinuity equilibrium and $\boldsymbol{w}^i$ given on the element level the computation continues for an improved $\boldsymbol{u}^i$ on the system level. From Eq. (46) the current residual is given with

$${}^1\boldsymbol{r}_I = \boldsymbol{p}_I^i - \boldsymbol{f}_I\left({}^1\boldsymbol{u}_I^i, \boldsymbol{w}^i\right) \tag{54}$$

and for $|{}^1\boldsymbol{r}_I| > 0$ the general Newton-Raphson iteration is performed with

$$\begin{aligned} \delta^{\nu+1}\boldsymbol{u}_I &= -\left.\frac{\partial \boldsymbol{r}_I(\boldsymbol{u}_I)}{\partial \boldsymbol{u}_I}\right|_{\boldsymbol{u}_I={}^{\nu}\boldsymbol{u}_I^i} \cdot {}^{\nu}\boldsymbol{r}_I \\ \Delta^{\nu+1}\boldsymbol{u}_I &= \Delta^{\nu}\boldsymbol{u}_I + \delta^{\nu+1}\boldsymbol{u}_I \\ {}^{\nu+1}\boldsymbol{u}_I^i &= \boldsymbol{u}_I^{i-1} + \Delta^{\nu+1}\boldsymbol{u}_I \end{aligned} \tag{55}$$

which is nested with $\boldsymbol{w}$-iterations on the element level. The Jacobian is determined as

$$\begin{aligned} \frac{\partial \boldsymbol{r}_I(\boldsymbol{u}_I)}{\partial \boldsymbol{u}_I} &= -\frac{\partial \boldsymbol{f}_I(\boldsymbol{u}_I, \boldsymbol{w})}{\partial \boldsymbol{u}_I} - \frac{\partial \boldsymbol{f}_I(\boldsymbol{u}_I, \boldsymbol{w})}{\partial \boldsymbol{w}} \cdot \frac{\partial \boldsymbol{w}}{\partial \boldsymbol{u}_I} \\ &= -\boldsymbol{K}_{T,uu} + \boldsymbol{K}_{T,uw} \cdot \mathcal{D}_{T,w} \\ &= -\mathcal{K}_{T,u} \end{aligned} \tag{56}$$

see Eqs. (37), (40), (43). System equilibrium is basically reached with $|{}^{\nu}\boldsymbol{r}_u| \approx 0$ and yields the solutions for the total displacements $\Delta \boldsymbol{u}_I, \boldsymbol{u}_I^i$ of all nodes and for the discontinuity degrees of freedom

$\Delta \boldsymbol{w}, \boldsymbol{w}^i$ for all elements. This leads to strains and strain increments with Eq. (19) and finally to bulk stresses at time t^i with a constitutive law. The solutions for the following time steps are derived in the same way whereby following the prescribed loading history.

2.5. Crack initiation, geometry and tractions

Crack formation is dependent on the loading history whereby crack initiation is ruled by predefined criteria. A Rankine criterion is used in the following, i.e. a crack initiates when a principal tensile stress exceeds the uniaxial tensile strength of the bulk material. The normal to the crack surface coincides with the direction of the respective principal stress.

Phenomena become complex from a phenomenological point of view after crack initiation. Mesoscopic crack development is characterized by (1) micro crack alignment, (2) micro crack enlargement, (3) crack bridging by aggregates, (4) macro cracking, Cracking evolves within the so called process band with a width of 2–3 times largest aggregate size, see Fig. 2. This is simplified with the fictitious or cohesive crack model (Hillerborg et al., 1976) in order to remain within the framework of continuum mechanics.

This model has to be related to finite elements. Element stresses are evaluated in element integration points. Numerical integration is performed with the Gaussian scheme with four sampling points for the 2D quad element currently under consideration. As the element size is chosen to be relatively small for FRCC specimen subject to the investigation – in the magnitude of [mm] and generally smaller than the crack band width – cracks are not allowed with respect to every integration point but they are placed in the geometric center of an element. Thus, a crack initiates when the center projection of the integration point largest principal stresses exceeds the uniaxial tensile strength whereby the normal to the crack surface coincides with the direction of centered principal stress. This yields the data x_0, y_0 and V^+, V^- for $\mathcal{H}$, see Eqs. (13, 15) and Fig. 1, to be used for the SDA extension of an element fulfilling the criteria during a loading history.

Crack directions are not constrained by already cracked neighbor elements, i.e. a crack contour extending over a series of elements is not enforced to be continuous. On the one hand the principal stress directions generally will not deviate too much within neighbored elements, on the other hand the computed sharp crack contour indicates an extended band for small computed crack width values. Resolution of finite width crack bands requires methods like gradient damage or phase fields with a much more refined discretization. The criteria for crack initiation are checked after each time step for each element, i.e. an explicit check is performed. This might lead to an overestimation of concrete tensile strength which can be controlled by the time step size. These assumptions about position, direction and check points to a large extent simplify the procedure. They also easily allow for an initiation of multiple cracks with the same center but different orientations.

Furthermore, tractions transmitted depending upon crack width have to be defined for the fictitious crack model. The general form has already been given with Eqs. (27) and (28). Regarding 2D this includes a normal component and a shear component. The behavior of the normal component has been investigated to a large extent allowing for a softening course as shown in Fig. 3 for normal crack tractions t_n depending on normal crack width w_n (Gopalaratnam and Shah, 1985; Reinhardt et al., 1986; Petersson, 1981). This is constrained by the maximum normal stress t_{ct} on crack initiation – basically the concrete uniaxial tensile strength –, the so called critical crack w_{cr} width where crack tractions come to zero and further the fracture energy

$$G_f = \int_0^{w_{cr}} t_n \, \mathrm{d}w_n \tag{57}$$

These values are generally assumed as material parameters to be determined from experiments. This approach is modified insofar as t_{ct}, G_f are used as input parameters and a parabolic $t_n - w_n$-relation

$$t_n = t_{ct}\left(\delta_n^2 - 2\delta_n + 1\right), \quad 0 \leqslant \delta_n = \frac{w_n}{w_{cr}} \leqslant 1 \tag{58}$$

is assumed with an extremal minimum in w_{cr}. Thus, the fracture energy is given with $G_f = \frac{1}{3} t_{ct} w_{cr}$. This yields a value w_{cr} for prescribed values G_f, t_{ct} generally conforming to experimental data which for w_{cr} anyway are hard to estimate regarding the background given in Fig. 2. The tangential stiffness is given with

$$\frac{\mathrm{d}t_n}{\mathrm{d}w_n} = \frac{t_{ct}}{w_{cr}}\left(2\delta_n - 2\right) \tag{59}$$

This describes the state of loading. Unloading is possible from all points of the loading path and follows a branch indicated in Fig. 3 with the point of initial unloading $(w_{n,u}, t_{n,u})$ connected to the origin. The pair $(w_{n,u}, t_{n,u})$ is a state variable comprising the preceding load history. The ratio $(t_{n,u}/w_{n,u})$ indicates the unloading stiffness and $(t_{n,u}/w_{n,u})\, w_n$ the crack traction with the current w_n on the unloading path. Crack closure is modeled with a penalty approach with a high constant positive stiffness in the range $w_n \leqslant 0$. Reloading elastically retraces crack closure and unloading up to the current $(w_{n,u}, t_{n,u})$ and continues along the loading path. This unloading,

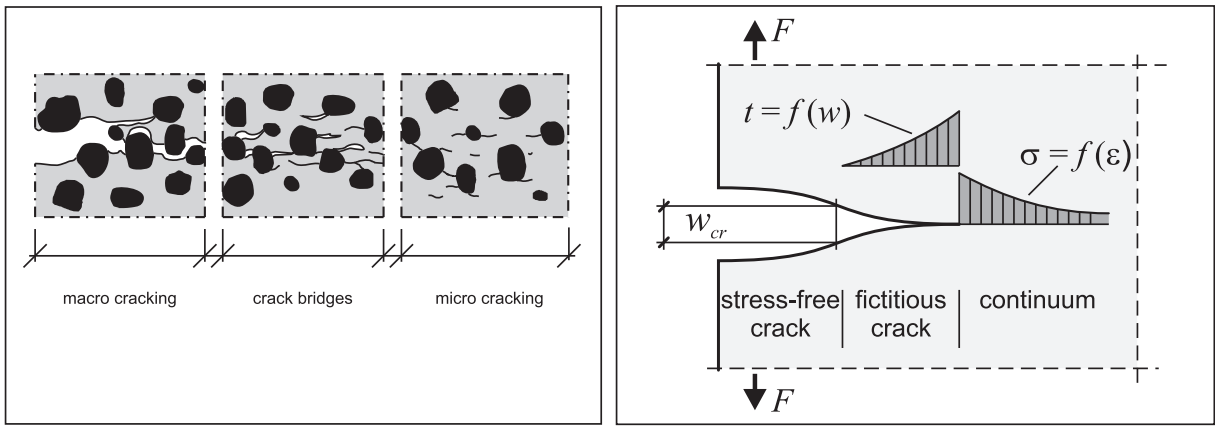


Fig. 2. a) Scheme of mesoscopic crack formation b) Fictitious crack model.

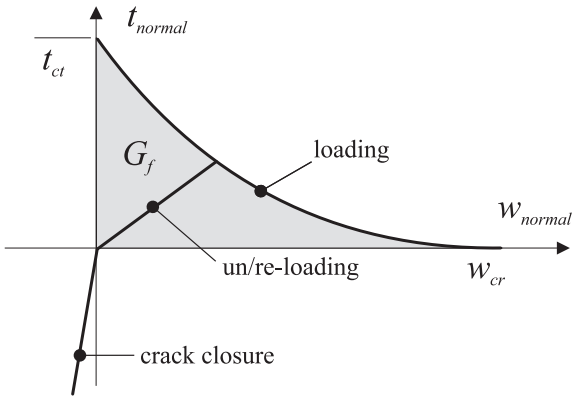


Fig. 3. Relation between normal components of crack traction – crack width.

crack closure, and reloading path is assumed among several other options due to its simplicity.

In contrast to the normal component much less knowledge is available for the shear component t_s depending on the crack sliding w_s. A simple shear retention

$$t_s = \alpha_s (1-\delta_n)^2 E_{bulk}\ w_s \tag{60}$$

is assumed for this purpose with the Young's modulus E_{bulk} of the bulk material and a shear retention factor α_s. The inclusion of the related normal crack width δ_n, see Eq. (58), scales the shear traction down with increasing normal crack width. The shear retention factor is assumed in a range $0 \leqslant \alpha_s \leqslant 0.01$ and subject to parameter sensitivity studies. The tangential stiffness is assumed with

$$\frac{\mathrm{d}t_s}{\mathrm{d}w_s} = \alpha_s (1-\delta_n)^2 E_{bulk} \tag{61}$$

The contribution $\mathrm{d}t_s/\mathrm{d}w_n$ is neglected in order to preserve general symmetry. A value $\alpha_s > 0$ generally proves to be necessary regarding convergence and stability of numerical computations. The relations of t_n, t_s depending on w_n, w_s and their tangential stiffness are originally formulated in a local coordinate system aligned to the crack orientation. Regarding Eqs. (27, 28) they remain – specifically for each cracked element – to be transformed into the global coordinate system to which the derivations of Sections 2.2 to 2.4 refer to.

A final point pertains with the order of Gaussian numerical integration to determine quantities like $\boldsymbol{f}_I \ldots$ and $\boldsymbol{K}_{T,uu} \ldots$. It is performed on the element level whereby results are assembled on the system level if required. This primarily concerns integrations over domains V of elements extended with SDA to describe cracks or a discontinuity of displacements. Such discontinuities generally also lead to discontinuities of stresses which might impair the precision of the Gaussian integration scheme. Bulk stress discontinuities should be attenuated due to equilibrating crack tractions upon the fulfillment of Eq. (22). Thus, the ordinary 2×2 integration for 2D quad elements is retained for SDA quad elements. This is used as a reference for parameter studies with varying integration orders in later investigations.

Furthermore, regarding $\boldsymbol{f}_w$, see Eq. (25), and $\boldsymbol{K}_{T,nn}$, see Eq. (29), numerical integrations have to be performed along the discontinuity contour A_d, see Fig. 1. With the linear discontinuity approach Eq. (13) and the at most quadratic approach for tractions, see Fig. 3, a 2-point Gaussian integration generally proves to be sufficient for the 2D setup.

2.6. Viscous regularization

Switches between loading and unloading branch of crack tractions are typical for very small normal crack width values w_n or spatially non–homogenous structures during a loading history whereby a crack initiation in a particular element often leads to internal stress redistributions and an unloading in neighbored cracked elements. As the tangential stiffness differs in sign, see Fig. 3, the Newton–Raphson iteration for the equilibrium on the element level, see Eqs. (49)–(52), tends to yield an oscillating behavior consecutively switching between the loading and unloading branches.

Two cases can be observed: a stationary residual oscillation with an upper bounded $|\boldsymbol{r}_w|$, see Eq. (49), and an unstable oscillation with strongly increasing and unbounded $|\boldsymbol{r}_w|$. While the first one generally is followed by convergence in later steps, the latter destabilizes the whole simulation and leads to a computation exit. This is typical for large systems. A stabilization may practically be reached by introducing a regularizing additional viscous contribution to the crack traction – crack width relation Eq. (27)

$$\begin{aligned} \boldsymbol{t}_d &= \boldsymbol{f}(\boldsymbol{w}) + \boldsymbol{t}_{d,vis} \\ \boldsymbol{t}_{d,vis} &= \eta_w \dot{\boldsymbol{w}} \\ \dot{\boldsymbol{t}}_{d,vis} &= \eta_w \ddot{\boldsymbol{w}} \end{aligned} \tag{62}$$

with a parameter η_w to reach a damping effect (Belytschko et al., 2000). The function $\boldsymbol{f}$ marks the quasi-static contribution according to Eqs. (58) and (60) transferred to the global system. Time derivatives of $\boldsymbol{w}$ are discretized in time with the one step Newmark-method (Bathe, 1996) with time integration parameters γ, β

$$\begin{aligned} \dot{\boldsymbol{w}}^i &\approx \tfrac{\gamma}{\beta\Delta t}\left[\boldsymbol{w}^i - \boldsymbol{w}^{i-1}\right] + \left(1-\tfrac{\gamma}{\beta}\right)\dot{\boldsymbol{w}}^{i-1} + \Delta t\left(1-\tfrac{\gamma}{2\beta}\right)\ddot{\boldsymbol{w}}^{i-1} \\ &= \tfrac{\gamma}{\beta\Delta t}\Delta\boldsymbol{w} + \left(1-\tfrac{\gamma}{\beta}\right)\dot{\boldsymbol{w}}^{i-1} + \Delta t\left(1-\tfrac{\gamma}{2\beta}\right)\ddot{\boldsymbol{w}}^{i-1} \\ \ddot{\boldsymbol{w}}^i &\approx \tfrac{1}{\beta\Delta t^2}\left[\boldsymbol{w}^i - \boldsymbol{w}^{i-1}\right] - \tfrac{1}{\beta\Delta t}\dot{\boldsymbol{w}}^{i-1} - \left(\tfrac{1}{2\beta}-1\right)\ddot{\boldsymbol{w}}^{i-1} \\ &= \tfrac{1}{\beta\Delta t^2}\Delta\boldsymbol{w} - \tfrac{1}{\beta\Delta t}\dot{\boldsymbol{w}}^{i-1} - \left(\tfrac{1}{2\beta}-1\right)\ddot{\boldsymbol{w}}^{i-1} \end{aligned} \tag{63}$$

as second order derivatives occur. The time integration parameters are generally chosen with $\gamma = 1/2,\ \beta = 1/4$ to have unconditional stability independent of Δt. This leads to

$$\begin{aligned} \dot{\boldsymbol{w}}^i &= \tfrac{2}{\Delta t}\Delta\boldsymbol{w} - \dot{\boldsymbol{w}}^{i-1} \\ \ddot{\boldsymbol{w}}^i &= \tfrac{4}{\Delta t^2}\Delta\boldsymbol{w} - \tfrac{4}{\Delta t}\dot{\boldsymbol{w}}^{i-1} - \ddot{\boldsymbol{w}}^{i-1} \end{aligned} \tag{64}$$

and firstly

$$\boldsymbol{t}_{d,vis} = \frac{2\eta_w}{\Delta t}\Delta\boldsymbol{w} - \eta_w \dot{\boldsymbol{w}}^{i-1} \tag{65}$$

The rate of the viscous crack traction is approximated in analogy to Eq. $(64)_1$

$$\dot{\boldsymbol{t}}^i_{d,vis} = \frac{2}{\Delta t}\Delta\boldsymbol{t}_{d,vis} - \dot{\boldsymbol{t}}^{i-1}_{d,vis} \tag{66}$$

Using Eqs. $(64)_2$, (66) for Eq. $(62)_3$ yields

$$\Delta\boldsymbol{t}_{d,vis} = \frac{2\eta_w}{\Delta t}\Delta\boldsymbol{w} - 2\eta_w\dot{\boldsymbol{w}}^{i-1} - \frac{\Delta t}{2}\eta_w\ddot{\boldsymbol{w}}^{i-1} + \frac{\Delta t}{2}\dot{\boldsymbol{t}}^{i-1}_{d,vis} \tag{67}$$

As $\dot{\boldsymbol{w}}^{i-1}, \ddot{\boldsymbol{w}}^{i-1}, \dot{\boldsymbol{t}}^{i-1}_{d,vis}$ are given and constant in the current setup an algorithmic tangential stiffness is derived with

$$\frac{\partial\Delta\boldsymbol{t}_{d,vis}}{\partial\Delta\boldsymbol{w}} = \frac{2\eta_w}{\Delta t}\boldsymbol{I} \tag{68}$$

with the identity matrix $\boldsymbol{I}$. The integration of this approach into the Newton–Raphson iteration on the element level, see Eqs. (49)–(53), is straightforward by adding $\boldsymbol{t}_{d,vis}$ from Eq. (65) to $\boldsymbol{t}_d$ in Eq. (25) and the tangential stiffness Eq. (68) to $\boldsymbol{C}_{Tw}$ in Eq. (28).

Summing up, the final tangential discontinuity material stiffness $\boldsymbol{C}_{Tw}$ from Eq. (28) has two additive contributions: the quasi-static part from Eqs. (59, 61) translated into the global system and the viscous part from Eq. (68). The first one potentially is negative definite due to the negative stiffness $\mathrm{d}t_n/\mathrm{d}w_n$, the second one is always positive definite. A negative definite sum generally impairs the Newton–Raphson equilibrium iteration. But the sum can always be made positive definite, i.e. regularized, by an appropriate selection of $\eta_w/\Delta t$. On the other hand the selection of a viscosity η_w for this viscous regularization approach is somehow arbitrary as no experimental evidence is currently available. It should be chosen such that it facilitates convergence behavior but has no significant impact on simulation results.

2.7. Embedded fibers with flexible bond

Major fiber properties were already described in Section 1. They act uniaxial without appreciable bending stiffness. Thus, they are modeled with finite truss elements. Series of truss elements should be allowed for an arbitrary placement within a surrounding continuum with own nodes independent of continuum nodes, see Fig. 4. Truss elements and continuum elements are coupled by special bond elements which are developed in the following. Displacements of truss elements are interpolated by

$$\boldsymbol{u}_t(\boldsymbol{x}) = \boldsymbol{N}_t(\boldsymbol{x}) \cdot \boldsymbol{u}_{tI} \tag{69}$$

in analogy to Eq. (2) but with their specific shape functions $\boldsymbol{N}_t$. Furthermore, displacements of continuum elements are interpolated according to Eq. (17)

$$\boldsymbol{u}(\boldsymbol{x}) = \boldsymbol{N}(\boldsymbol{x}) \cdot \boldsymbol{u}_I \tag{70}$$

in its full form for SDA or restricting to $\bar{\boldsymbol{u}}_I$ for other. Regarding so-called anchor points $\boldsymbol{x}_{a,i}$ placed along the truss elements, see Fig. (4), this yields a difference of displacements or slip

$$\begin{aligned} \boldsymbol{s} &= \boldsymbol{u}_t(\boldsymbol{x}_{a,i}) - \boldsymbol{u}(\boldsymbol{x}_{a,i}) \\ &= \begin{bmatrix} \boldsymbol{N}_t(\boldsymbol{x}_{a,i}) & -\boldsymbol{N}(\boldsymbol{x}_{a,i}) \end{bmatrix} \cdot \begin{pmatrix} \boldsymbol{u}_{tI} \\ \boldsymbol{u}_I \end{pmatrix} \\ &= \boldsymbol{B}_b(\boldsymbol{x}_{a,i}) \cdot \begin{pmatrix} \boldsymbol{u}_{tI} \\ \boldsymbol{u}_I \end{pmatrix} \end{aligned} \tag{71}$$

for a particular anchor point derived from the nodal displacements of the respective truss element and the nodal displacements of neighbored continuum elements. This also constitutes the kinematic variable of the bond element assigned to the anchor point $\boldsymbol{x}_{a,i}$. The slip induces bond forces

$$\boldsymbol{t}_b = \boldsymbol{t}_b(\boldsymbol{s}) \tag{72}$$

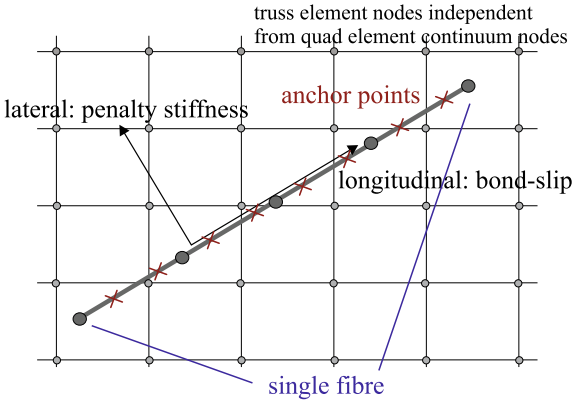


Fig. 4. Fiber discretization embedded in continuum.

as counteracting couple for the truss element on the one hand and the underlying continuum on the other hand. The relation is generally nonlinear. It may be considered as further material relation in analogy to Eqs. (5, 27) and is also assumed to be known. An incremental form

$$\dot{\boldsymbol{t}}_b = \boldsymbol{C}_{Tb}(\boldsymbol{s}) \cdot \dot{\boldsymbol{s}} \tag{73}$$

is used in the following in analogy to Eqs. (8) and (28) which is related to the global coordinate system. Regarding a local system aligned to the truss direction the bond-slip relation is assumed such that a lateral slip or intersection is basically avoided by a penalty term and the longitudinal slip reproduces a given bond behavior. This is generally connected with an upper limit for the longitudinal bond force, i.e. a bond strength.

Regarding the discretization a bond force couple – one part applied to a truss element, the other part applied to a continuum element – is introduced as point load at $\boldsymbol{x}_{a,i}$ leading to a couple of nodal forces

$$\boldsymbol{f}_b = \begin{pmatrix} \boldsymbol{f}_{bt} \\ \boldsymbol{f}_{bc} \end{pmatrix} = \boldsymbol{B}_b^T \cdot \boldsymbol{t}_b \tag{74}$$

for the truss element $\boldsymbol{f}_{bt}$ on the one hand and for the neighbor continuum element $\boldsymbol{f}_{bc}$ on the other hand. This is in analogy to Eqs. (8, 35) whereby the integration over a domain is not required as bond is implemented through single forces. This is linearized with

$$\begin{aligned} \dot{\boldsymbol{f}}_b &= \boldsymbol{B}_b^T \cdot \boldsymbol{C}_{Tb} \cdot \boldsymbol{B}_b \cdot \begin{pmatrix} \dot{\boldsymbol{u}}_{tI} \\ \dot{\boldsymbol{u}}_I \end{pmatrix} \\ &= \boldsymbol{K}_{T,b} \cdot \begin{pmatrix} \dot{\boldsymbol{u}}_{tI} \\ \dot{\boldsymbol{u}}_I \end{pmatrix} \end{aligned} \tag{75}$$

for a particular bond element using Eqs. (73, 71). As embedded fibers do not have displacement boundary conditions externally prescribed a minimum number of two anchor points $\boldsymbol{x}_{a,i}$, i.e. a minimum of two bond elements is required per truss element to avoid rigid body movements. They are conveniently placed in truss element integration points.

Nodal forces $\boldsymbol{f}_b$ and the tangential stiffness $\boldsymbol{K}_{T,b}$ can be assembled on the system level for each bond element: $\boldsymbol{f}_b$ is added to the assembled $\boldsymbol{f}_I$, see Eq. (8), $\boldsymbol{K}_{T,b}$ is added to the assembled $\mathcal{K}_{T,u}$, see Eq. (43), according to the mappings of the underlying truss and continuum elements. Thus, the introduction of bond elements seamlessly fits into the solution procedure described in Section 2.4.

A standard 2D truss element is given with the isoparametric two-node element with two degrees of freedom per node, i.e. four degrees of freedom with shape functions, see Eq. (69)

$$\begin{aligned} \boldsymbol{N}_t &= \begin{bmatrix} N_{t1}(\xi) & 0 & N_{t2}(\xi) & 0 \\ 0 & N_{t1}(\xi) & 0 & N_{t2}(\xi) \end{bmatrix} \\ N_{t1}(\xi) &= \tfrac{1}{2}(1-\xi) \\ N_{t2}(\xi) &= \tfrac{1}{2}(1+\xi) \end{aligned} \tag{76}$$

with the local coordinate $-1 \leqslant \xi \leqslant 1$. This implies constant longitudinal strains and stresses. An enhanced approach is chosen for quadratic longitudinal displacements with

$$\begin{aligned} \boldsymbol{N}_{t\prime} &= \begin{bmatrix} N_{t3}(\xi) & 0 & N_{t4}(\xi) & 0 & N_{t5}(\xi) \\ 0 & N_{t1}(\xi) & 0 & N_{t2}(\xi) & 0 \end{bmatrix} \\ N_{t3}(\xi) &= \tfrac{1}{2}(1-\xi) - \tfrac{1}{2}(1-\xi^2) \\ N_{t4}(\xi) &= \tfrac{1}{2}(1+\xi) - \tfrac{1}{2}(1-\xi^2) \\ N_{t5}(\xi) &= 1-\xi^2 \end{aligned} \tag{77}$$

introducing a fifth nodal degree of freedom for longitudinal displacements. This at first is valid in a coordinate system aligned with the first displacement direction $u_{x\prime}$ aligned to the truss element axis. This leads to an aligned $\boldsymbol{B}$-matrix, compare Eq. (2)

$$\boldsymbol{B}_{t\prime} = \frac{1}{L}\left[2\xi - 1 \quad 0 \quad 2\xi + 1 \quad 0 \quad -4\xi\right] \tag{78}$$

with an element length L according to well-known rules of isoparametric finite elements. The aligned direction is rotated by an angle φ to the global direction, see Fig. 4. As $\boldsymbol{u\prime} = \boldsymbol{T} \cdot \boldsymbol{u}$ with

$$\boldsymbol{T} = \begin{bmatrix} \cos\varphi & \sin\varphi & 0 & 0 & 0 \\ -\sin\varphi & \cos\varphi & 0 & 0 & 0 \\ 0 & 0 & \cos\varphi & \sin\varphi & 0 \\ 0 & 0 & -\sin\varphi & \cos\varphi & 0 \\ 0 & 0 & 0 & 0 & 1 \end{bmatrix} \tag{79}$$

the final $\boldsymbol{B}$-matrix is given with

$$\boldsymbol{B}_t = \boldsymbol{B}_{t\prime} \cdot \boldsymbol{T} \tag{80}$$

leading to linear strains with an additional degree of freedom not assigned to a node. Regarding embedded truss elements this enhanced approach yields the same behavior as fully quadratic elements but with fewer degrees of freedom.

Both approaches – linear or quadratic – cover a range of reinforcement types from long single rebars arranged in a regular pattern each discretized with a large number of elements up to a large number of short fibers with random orientation each discretized with a small number of elements. It works in 2D and 3D and basically with all types of finite elements including the SDA approach described above. Truss elements might be replaced with beam elements in case of thick fibers with bending stiffness. This introduces rotational degrees of freedom into the system beneath translational. A rebar bending, e.g., might become relevant as so-called dowel action upon crossing of cracks.

3. Model validation

3.1. Solution basics

The simulation model basically includes nonlinear behavior for the bulk material, cracks, the fiber material and the bond connecting them. As the tensile behavior of FRCC is under focus within the current investigation a linear elastic behavior with limited tensile strength is assumed, multiaxial for the bulk material and uniaxial for the fibers. Reaching the maximum bulk tensile strength is connected with a nonlinear softening behavior, see Fig. 3. The case of unloading down to crack closure with following reloading is allowed, as this is generally seen during a loading history in specimen with random fiber orientations and spatial inhomogeneities. Brittle tensile failure is assumed for the fiber material with element erosion when the tensile strength is exceeded. Longitudinal bond is assumed as nonlinear with a limited bond strength followed by a softening, i.e. increasing longitudinal slip with decreasing longitudinal bond stresses. The corresponding relations are derived from experimental data. Lateral bond is constrained with an elastic penalty approach in order to avoid mutual intersection.

Although the described approaches allow for an immediate extension to 3D the following discussions are restricted to 2D examples which already show basic characteristics. Four node plane stress quadrilateral elements are used for the continuum and two node elements, with and without enhancement, for the truss elements. A maximum of two cracks is allowed for a single continuum element whereby a fixed crack approach is used. Rotating cracks might be regarded with a variation of domains V^+, V^- depending on a load history. This would lead to a further source of nonlinearities and is currently avoided.

Furthermore, the investigations are restricted to quasi-static cases. Extension to implicit dynamics is possible with the standard approaches and actually was already implemented. Due to the above mentioned physical nonlinearities an incrementally iterative approach is chosen as solution procedure with equilibrium iterations performed with the Newton-Raphson method used within each loading increment, each on the system level and the element level, see Section 2.4.

3.2. Tensile behavior of one-element model

To start with, the basic tensile softening behavior after cracking is demonstrated with continuum one-element examples. A setup of boundary conditions and loading is shown in Fig. 5. The loading is applied as prescribed nodal displacements. The assumed material properties are given in Table 1. A crack viscosity, see Section 2.6, is not regarded for the one-element simulations: $\eta_w = 0$. Variations are performed with the following loading scenarios:

1. Uniaxial tension with cracking and softening up to zero normal crack tractions.
   Loading is applied as prescribed horizontal displacements of nodes 2 and 3 in the horizontal direction whereby exceeding the critial crack width with zero stresses.
2. Uniaxial tension with cracking and softening up to some residual crack tractions followed by orthogonal tension with orthogonal cracking and softening.
   Loading is applied as in Scenario 1 up to some residual tensile stress. Further loading is applied with vertical displacements of nodes 3 and 4 up to the critical crack width of the secondary horizontal crack whereby the prescribed horizontal displacement is kept.
3. Uniaxial tension with cracking and softening up to some residual crack tractions followed by combined shear and orthogonal tension with a second crack and softening corresponding to Willam's test (Willam et al., 1989; Pivonka et al., 2004).
   Loading is applied as in Scenario 1 up to some residual tensile stress. Further loading is applied with vertical and horizontal displacements of nodes 3 and 4 whereby node 4 is released from kinematic boundary conditions. Furthermore, the horizontal displacement of node 2 is continued. Strains $\epsilon_{xx}, \epsilon_{yy}, \epsilon_{xy}$ uniformly increase in this second loading stage whereby the state of strain is homogeneous within the continuum element.

Each scenario is investigated with a square element with two different element sizes of 1 mm and 10 mm edge length.

3.2.1. Uniaxial tension

Fig. 6 shows the computed stress-displacement curves for scenario 1 for both element sizes. The total displacements consist of the contribution of the horizontal strains and the crack width. This

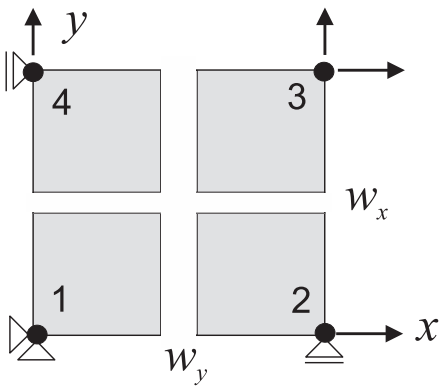


Fig. 5. Single continuum element setup.

Table 1
Fine grained concrete property values.

Young's modulus E	$[N/mm^2]$	29000
Poisson's ratio ν	–	0.2
Tensile strength f_{ct}	$[N/mm^2]$	3.8
Fracture energy G_f	[N/mm]	$100 \cdot 10^{-3}$
Critical crack width w_{cr}	[mm]	0.079

starts with strains only up to the point where the prescribed tensile strength is reached. Up to this the elongation of the large element is 10 times higher compared to the small element as the same stresses and strains arise. This becomes visible with a clipping as is shown in Fig. 6b. Cracking is not precisely initiated with the concrete tensile strength but with a slight overshoot due to the explicit checking procedure, see Section 2.5. During softening the elongation increases due to the increasing crack width with decreasing crack tractions according to Fig. 3.

The crack traction directly corresponds to the continuum stress which is connected to decreasing strains. But the corresponding length reduction is by far exceeded by the increasing crack width. Stresses and strain become zero when the elongation reaches the critical crack width, see Table 1. This is the same for both element sizes. The integrals of the stress-displacement curves of Fig. 6 include small contributions of the elastic energies stored until reaching the tensile strength and released through softening. Besides that the integrals or fracture energy are the same for both element sizes. This basically proves the objectivity of SDA with respect to finite element discretization without additional regularization.

3.2.2. Biaxial tension

Biaxial tension results are shown in Fig. 7 again as stress-elongation curves whereby the horizontal and vertical curves share the same diagram. But they occur for different periods of the loading history with delayed secondary cracking which implies a load induced anisotropy. Curves for the horizontal and vertical elongation basically coincide up to the intermediate point where the horizontal elongation remains stationary. The behavior in each direction is the same as with the uniaxial tension. The loading step size of the simulation is increased compared to the example of Section 3.2.1. Thus, the concrete tensile strength overshoot due to explicit crack initiation checking increases. Furthermore, elastic deformations – aligned with stresses and from Poisson effects – to a large degree become not obvious due to large crack openings.

The results for the elements sizes differ insofar as the elastic elongations prior to cracking differ proportional to the element size as was already discussed with uniaxial tension. But the fracture energy is the same for both element sizes. Finally, a decoupling of orthogonal behavior is seen, i.e. failure and tension softening in one direction do not influence the tensile behavior in the orthogonal direction. This results from the assumed isotropic elasticity of the continuum before cracking. Such a behavior might be questionable in the compressive range, but is assumed as appropriate for predominant tension.

3.2.3. Biaxial tension combined with shear

A last case of homogeneous behavior is discussed with biaxial tension combined with shear as has been described with loading scenario 3. Results are shown in Fig. 8 with all three stress components of plane stress states given depending on the loading time. As before elastic behavior is hardly obvious due to predominant crack width openings. The first stage of loading up to time 0.5 is characterized by uniaxial horizontal stresses σ_{xx}.

In the second stage this is followed by ongoing horizontal tensile loading combined with orthogonal tension and horizontally applied shearing. A second crack initiates relatively fast from orthogonal tension and is nearly orthogonal to the first crack. Ongoing prescribed displacements lead to initially increasing shear stresses and a corresponding rotation of principal strains and stresses. Continuum stresses $\sigma_{xx}, \sigma_{yy}, \sigma_{xy}$ correspond to crack tractions t_n, t_s, see Section 2.5, according to the discontinuity equilibrium condition Eq. $(36)_2$. As crack tractions have to go down to zero with increasing crack width, see Fig. 3 and Eq. (60), continuum stresses also go down to zero during the loading history, see Fig. 8. Thus, the basic criteria of Willam's test – tensile strength is not exceeded and all stresses end up with zero (Pivonka et al., 2004) – are fulfilled. An intermediate maximum value of the continuum shear stress σ_{xy} is implied. As its value depends on the prescribed shear retention factor α_s, see Eq. (60), a range for the shear retention factor may be calibrated from a reasonable range of maximum shear stresses. It is assumed with $\alpha_s = 0.01$.

Differences between the element sizes occur insofar, as initial convergence problems on the element level can be seen after second crack initiation for the large element size with small normal crack width values w_n. There is jumping back and forth to observe between loading and unloading branch as has been addressed in Section 2.6. But the residual remains bounded and convergence behavior is regained after a few steps. The occurrence is indicated in Fig. 8b. The following differences in stress relations arise from different prescribed strain relations as the prescribed displacements are the same for the small and large element simulations.

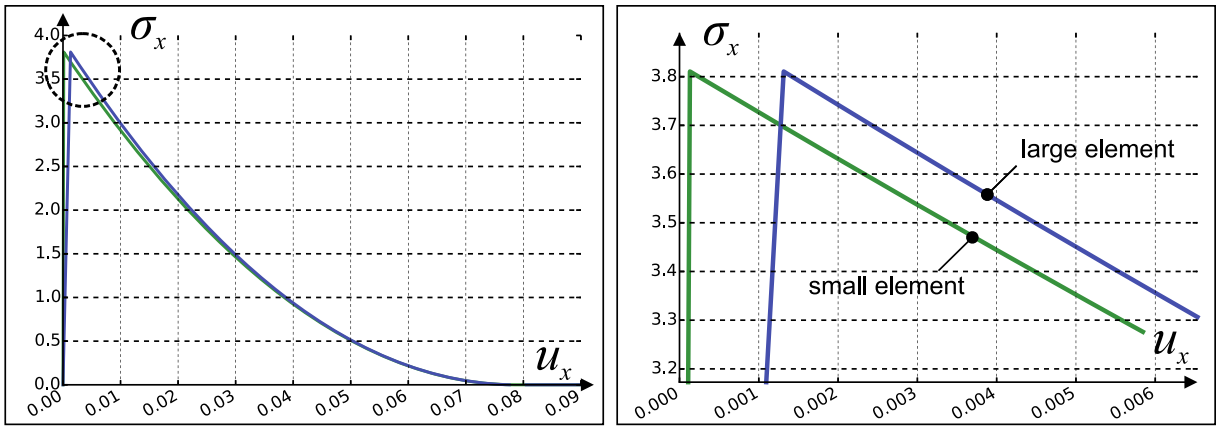


Fig. 6. Stress-elongation $[N/mm^2 - mm]$ for uniaxial tension a) long shot b) clipping from peak.

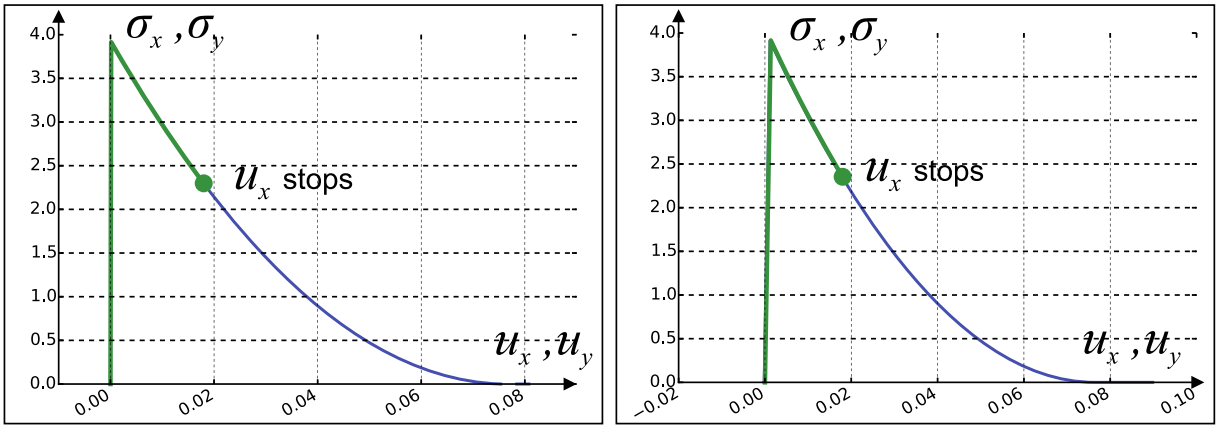


Fig. 7. Stress-elongation for biaxial tension [N/mm² – mm] a) small element b) large element.

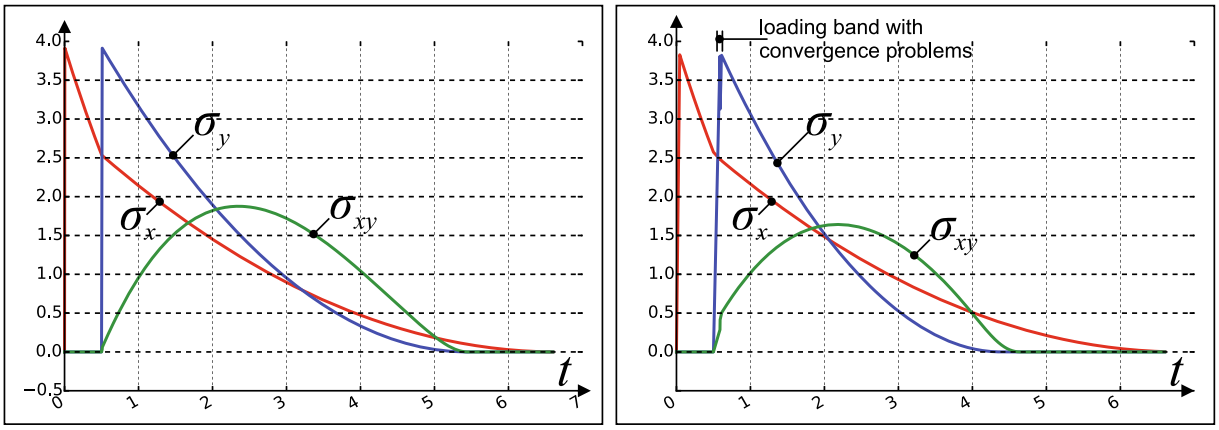


Fig. 8. Stress components N/mm² depending on loading time for biaxial tension combined with shear (Willams's test) a) small element b) large element.

3.3. Bond behavior of single fibers

Basic fiber properties have already been described in Section 1. Typical property values as they also used for the following numerical simulations are given in Table 2 whereby the strength is reduced compared to nominal values corresponding to practical experience. The simulation model allows for a wide range of these values. Brittle failure is assumed, i.e. a truss element is eroded when its stress exceeds the fiber tensile strength. Fibers interact with the cement matrix via bond. The bond behavior of single fibers is discussed with two cases in the following:

1. Single fiber fully embedded in an elastic continuum exposed to homogeneously applied tension.
2. Single fiber pulled out of an elastic continuum.

The continuum is assumed to have an unlimited tensile strength in both cases in order to reach undisturbed bond. A key item is given with the bond stress-slip relation for longitudinal flexible bond as part of Eq. (72).

Within the current mesoscopic framework this has to base on experimental data for pullout of single fibers in fine grained concrete blocks. Such experiments are difficult to perform due to the small dimensions of fibers but are basically available (Curosu et al., 2017; Curosu et al., 2016). As they are characterized by relatively large scatter mean data are used for the following. A typical course formulated as spline is shown in Fig. 9. The same is used for the negative range with a reversal of signs of slip and bond stress. It

Table 2
Fiber property values.

Young's modulus E_f	[N/mm²]	80 000
Tensile strength f_f	[N/mm²]	1 600
Length L	[mm]	6/10
Diameter ø	[mm]	0.02
Cross sectional area A_f	[mm²]	$3.14 \cdot 10^{-4}$
Failure load P_{fu}	[N]	0.5

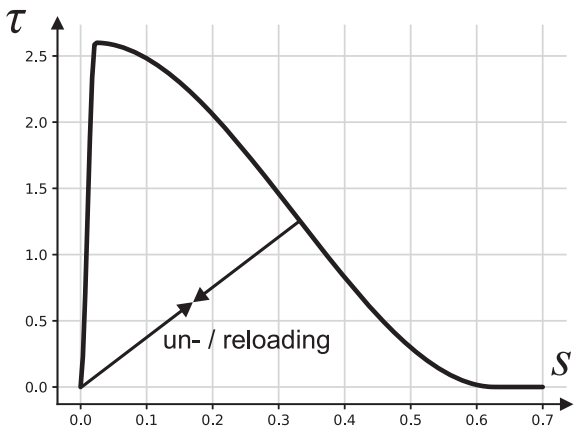


Fig. 9. Bond law with bond stresses [N/mm²] depending on slip [mm].

is characterized by an initial elasticity, maximum bond stress at a prescribed slip and a constant residual bond stress from another prescribed slip on. The residual stress is assumed with nearly zero to cover fiber pullout at least approximately. A precise modeling of fiber pullout would require a large displacement approach which exceeds the scope of the current small displacement assumption and has to be devoted to further work. Bond stress τ has a unit $[\mathrm{N/mm^2}]$. It is advantageously transformed into a stress flow T with a unit [N/mm] by multiplying it by fiber circumference U_f

$$T = U_f \tau = 2\sqrt{\pi A_f}\,\tau \tag{81}$$

derived from, e.g., the fiber cross sectional area A_f. This is applied for nodal forces in Eq. (74) and compensates for thickness variations of an underlying 2D continuum.

Un- and reloading follow lines connecting the point of unloading with the origin. Unloading introduces the current pairs of (maximum slip, corresponding bond stress) and (minimum slip, corresponding bond stress) as state variables of bond. Furthermore, a relation between lateral stresses and slips has to be made as completing part of Eq. (72). A linear penalty approach is used with a high lateral stiffness in the range of $1 \cdot 10^6$. This yields lateral slips which by absolute value are by dimensions lower compared to the longitudinal slips. Longitudinal and lateral relations are local and have to be transformed into the global system for an arbitrary fiber orientation.

A discretization is chosen with 10 two node enhanced truss elements, see Eqs. (77)–(80), for a single fiber of 10 mm length. The element size of the underlying continuum should roughly be adjusted to a truss element length of 1 mm. Thus, quad elements of 1 mm edge length are chosen as reference in 2D.

3.3.1. Fully embedded fiber

Dimensions and discretization are shown in Fig. 10a together with boundary conditions. A loading is given with uniform prescribed displacements of the right edge leading to longitudinal tension. As the bulk material is assumed as linear elastic without limited tensile strength a high loading is applied with a final mean strain of $6.7 \cdot 10^{-3}$. Corresponding fiber stresses are shown in Fig. 10b with longitudinal stresses σ and bond stresses τ along the fiber length x. A typical behavior of a reinforcement embedded in continuum can be seen: zero longitudinal stresses at the ends and an intermediate maximum longitudinal stress connected by bond stresses with maximum absolute values and switched sign at the ends and intermediate zero. The spatial derivative of longitudinal stresses – scaled by some constant factor – corresponds to the derivative of the bond stresses due to equilibrium conditions for the fiber cutout.

3.3.2. Fiber pullout

The discretization is the same as with the fully embedded fiber whereby its longitudinal position is moved to the right edge with a small fiber section outstanding, see Fig. 11. The loading is applied with the prescribed displacement of the right hand outstanding node of the fiber. Prescribed displacement is increased such that the fiber's failure load, see Table 2, is nearly reached. The computed fiber stresses along the fiber length for this final state are shown in Fig. 12a. In contrast to the fully embedded fiber both stresses start from zero at the left hand side and reach maximum values at the pulled right hand side. Bond stresses attain their prescribed maximum value, along some fiber length according to the prescribed bond law, see Fig. 9. All curves are multilinear due to linear interpolation between integration point values of truss elements. This becomes evident with the computed bond stress in Fig. 12a. Finally, Fig. 12b shows the computed pullout force–displacement curve of the fiber's r.h.s. node. This is slightly nonlinear whereby the fiber reaches its nominal strength, see Fig. 13a and Table 2, connected with a brittle fiber failure. The corresponding computed load, see Fig. 13b, slightly exceeds the fiber failure load as some additional bond stress is projected into the r.h.s nodal force of the r.h.s element. Bond strength is also reached, see Fig. 9 and Fig. 13a, but ranges only slightly into the softening range. Fiber pullout is not covered by the model due to the current limitation to small displacements. While strains or stresses are not accessible with experimental measurements – in contrast to simulation – experimental load–displacement curves are available, although with large scatter, and can be compared to the computations (Curosu et al., 2017; Curosu et al., 2016). Based on micromechanical behavior they serve as a first lead for a reverse estimation of bond laws, see, e.g. Fig. 9. A detailed discussion of the influence of bond laws on macroscopic behavior and their validation has to be devoted to following work.

A significant question with respect to later simulation with a very large number of fibers ($\approx 10^4$) concerns the required nominal fiber discretization quality. A comprehensive discussion would exceed the scope of the paper. First insights should be given a reduction of elements per fiber from 10 to 5 whereby using a linear approach for the longitudinal truss displacements leading to constant longitudinal strains and stresses within a single truss elements. This is applied with the fiber pullout simulation. Comparative results are shown in Fig. 13a for fiber stresses and in Fig. 13b for pullout force-displacement curves. Stresses on neighbored integration points are connected by straight lines, even

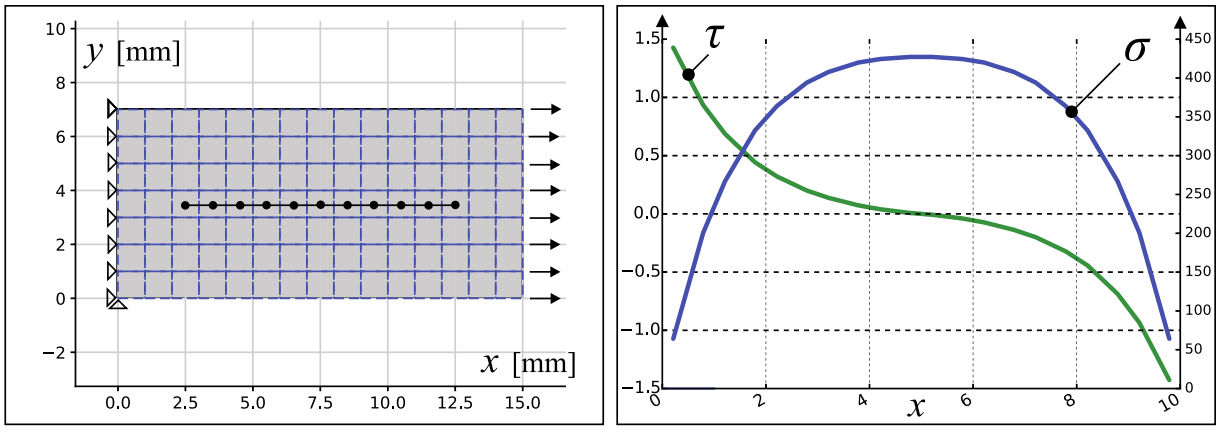


Fig. 10. Fully embedded fiber a) system and discretization b) final fiber and bond stresses $[\mathrm{N/mm^2}]$ along fiber length [mm].

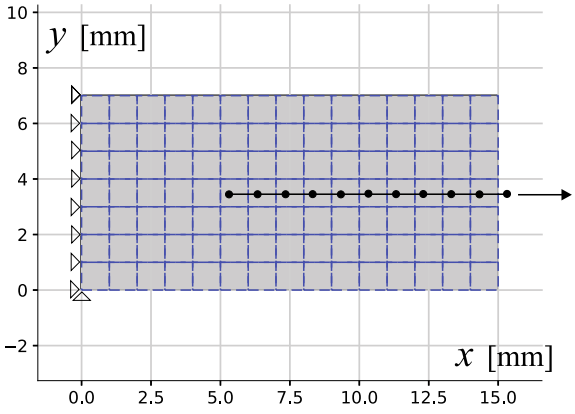


Fig. 11. System and discretization for fiber pullout.

in case of neighbored elements. This distorts the representation of longitudinal stresses of linear truss elements. Furthermore, extremal longitudinal stresses are balanced by the constant stress approach. On the other hand, bond stresses vary within a linear element as slips are not same for two different anchor points, see Fig. 4, and agree to large extent between the coarse linear and the fine quadratic approach. Thus, the difference between pullout force–displacement curves is minimal and the coarse approach will be chosen as reference for the following simulations with a large number of degrees of freedom.

In the illustrative examples in Sections 3.3.1 and 3.3.2 the fiber and the underlying continuum elements were aligned, however, it can be with any arbitrary direction as shown in Fig. 15.

3.4. Simulation of FRCC experiment

The simulation of an FRCC notched dog-bone specimen which was experimentally investigated is discussed as final example (Shehni et al., 2019). The experimental setup for an unnotched but otherwise identical specimen is shown in Fig. 14. The thickness of the specimen was chosen very thin in the mid region with $t = 3.5$ mm in order to approximate 2D conditions. The side view dimensions of the specimen's mid region are given in Fig. 15a. The fine grained concrete properties of the specimen determined with standard methods are again listed in Table 1, the fiber properties in Table 2. Fiber length is given with 6 mm and fiber content with 2 % of volume. The loading of the experimental specimen was applied by displacement control of the upper face while the lower face was fixed. Two nominally same notched specimen were tested and load–displacement curves determined.

The discretization of the 2D simulation model restricts to a center segment in order to reduce the problem size and is schematically shown in Fig. 15a. It is discretized with 1560 quad continuum elements with a thickness of $t = 0.1$ mm. With the given fiber content and single fiber volume of $1.88 \cdot 10^{-3}\,\text{mm}^3$ this leads to a total number of 1698 fibers for the simulation model. The position and orientation of the fibers, see Fig. 15b, is assumed as random with some constraints: the inclination of fibers is

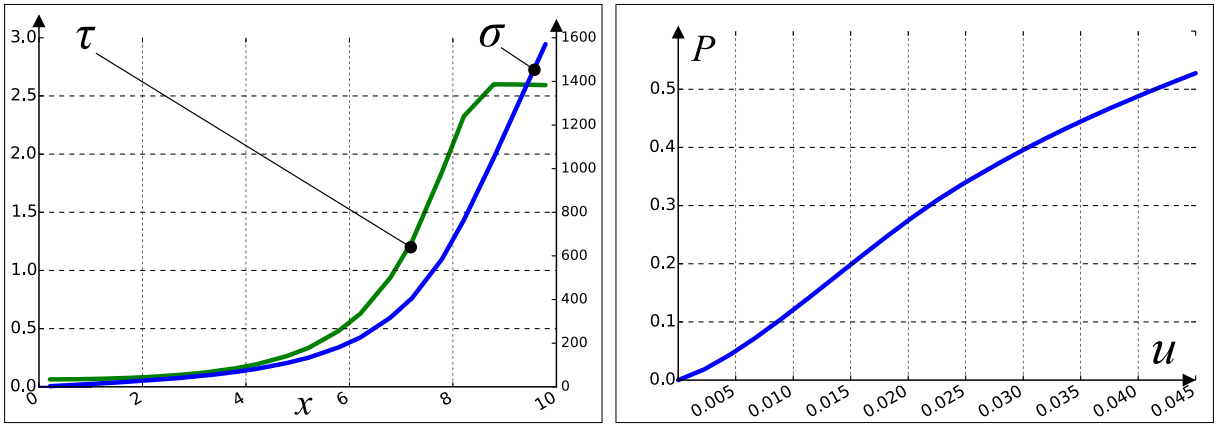


Fig. 12. Fiber pullout a) stresses $[\text{N/mm}^2]$ along fiber length [mm] b) pullout force-displacement curve [N – mm].

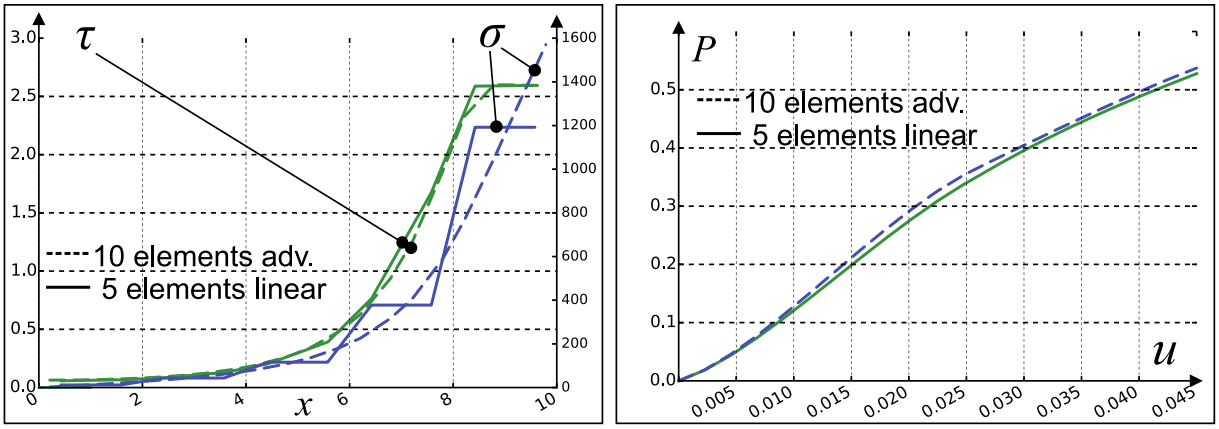


Fig. 13. Comparison fiber pullout a) stresses $[\text{N/mm}^2]$ along fiber length [mm] b) pullout force-displacement curve [N – mm].

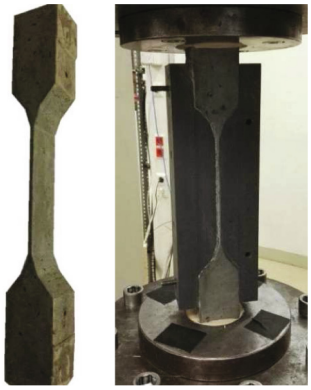


Fig. 14. FRCC experimental specimen (Shehni et al., 2019).

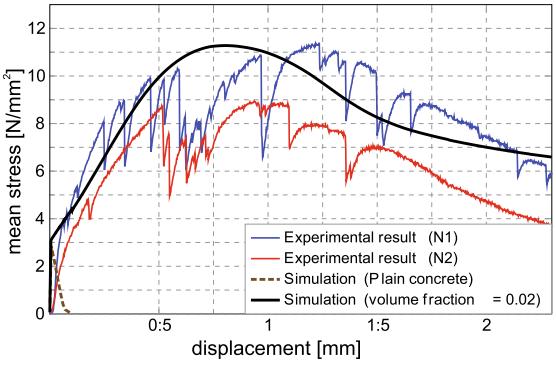


Fig. 16. FRCC mean stress – displacement results.

restricted within a range of ±5 degrees from the vertical. This corresponds to a survey of fibers within the experimental specimen. Besides that fiber arrangement is ruled by random methods. A single fiber is discretized with five constant stress truss elements, see Section 3.3.2. The whole simulation model includes 23 046 degrees of freedom. In contrast to one-element and single fiber simulations a viscous regularization, see Section 2.6, is required in order to avoid premature destabilization of the computation. A viscosity value combined with an initial loading time step of

$$\eta_w = 10\,\frac{\mathrm{N}}{\mathrm{mm}^2}\,\frac{\mathrm{s}}{\mathrm{mm}}, \qquad \Delta t = 0.001\,\mathrm{s} \tag{82}$$

is chosen for this purpose. Comparing this with simulations with $\eta_w = 0$ the differences are more or less insignificant as far as the latter provides reasonable data. The shear retention factor, see Eq. (60), is assumed with $\alpha_s = 0.01$ with fixed cracks and secondary cracking allowed.

As the loading is applied with vertical prescribed displacements, see Fig. 15a, reaction forces come as results and yield a computed load-displacement curve to be compared with experimental results. Due to the different length of the simulation model and the experimental model the displacement base of the experiments has to be adjusted to reach comparable displacements for the discretized notched center part. Load–displacement results from simulation and experiments are shown in Fig. 16, whereby loading is expressed in terms of mean stress according to common convention. An overall good agreement can be seen between experiment and simulation taking into account the experimental scatter. Simulation results for a plain concrete specimen without fibers but otherwise unchanged are also shown in Fig. 16. FRCC behavior is characterized by highly increased tensile strength and a superior ductile behavior compared to plain concrete. Comparing FRCC experiment and simulation characteristic items are commented as follows:

- Initial stiffness of the experimental specimen is significantly lower compared to simulation. This is attributed to the precracking of the very thin specimen, see Fig. 14, arising during handling before testing.
- Experimental curves show a distinct roughness whereby single spikes are hypothetically assigned to particular cracking events. As the number of spikes is much lower than the number of final cracks these particular events presumably belong to instantaneously larger cracks with localizations arising from the actual scatter of material properties, i.e. matrix tensile strength, bond properties and fracture energy. Dynamic phenomena presumably also come into play with these effects. Random fields and short time dynamics are not covered by the current simulation model.
- The simulation yields less decrease of stresses in the later softening range. This range is experimentally characterized by significant fiber pullout and single localizations. As the simulation model assumes small displacements the reproduction capabilities for fiber pullout are limited. Some compensation was tried with the assumption of the bond law with nearly zero residual friction, see Fig. 9, although this does not bring down the simulated loading to the experimental levels.

The load-displacement characteristics indicate global behavior. In contrast to experiments the simulation provides local results for

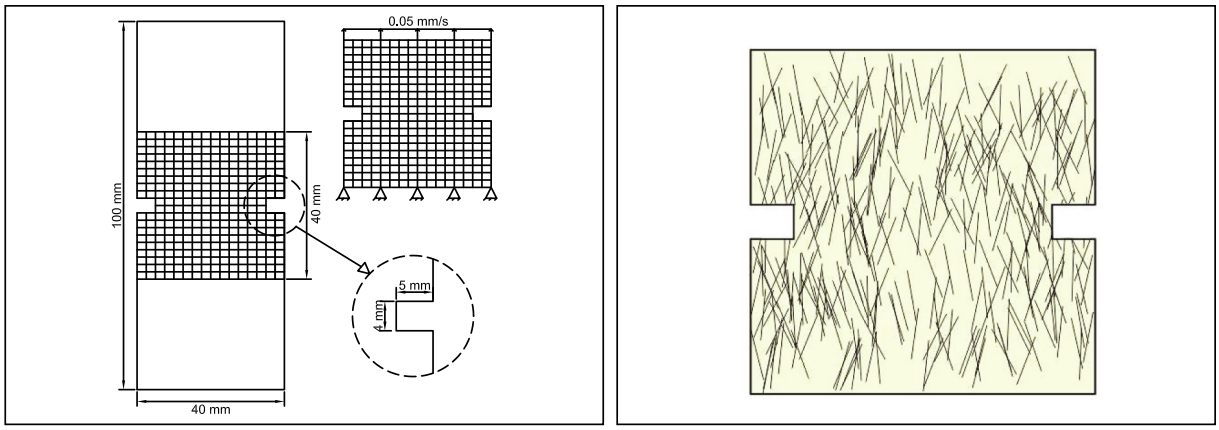


Fig. 15. FRCC simulation model a) mid region of dogbone with scheme of discretized center segment b) scheme of random fiber placement.

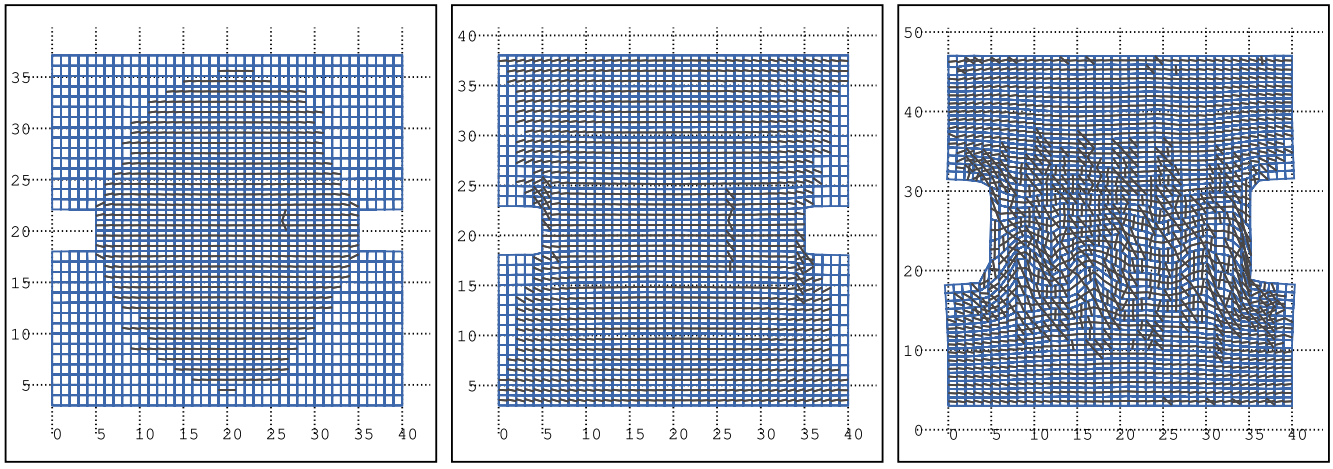


Fig. 17. FRCC simulation crack pattern results (displacements scaled by 10) a) $u = 0.01$ mm b) $u = 0.10$ mm c) $u = 1.00$ mm.

the whole loading history, e.g. matrix strains and stresses, cracking patterns, crack width, dissipated fracture energy, fiber and bond stresses and fiber failure events. A comprehensive presentation would exceed the scope of the paper. Thus, it is limited to the development of crack patterns, which are shown in Fig. 17 on the deformed mesh geometry for three prescribed displacements. The last shown crack pattern for $u = 1.0$ mm indicates a state shortly after maximum loading on the softening branch, see Fig. 16. A crack fully intersects an element through its center by definition, see also Section 2.5, and is indicated by a thicker dark gray line. Although outer geometry and boundary conditions are symmetric with respect to the vertical and horizontal center lines symmetry is not preserved in the simulation results due to random positions of fibers. Computed crack contours spreading over neighbored elements are not continuous but slightly deviate in their orientation. The interpretation of this simulation property has also been discussed in Section 2.5. Secondary cracking is constrained by a minimum deviation of 45 degrees compared to primary cracking orientation and occurs relatively soon, see Fig. 17b. This introduces some bias into secondary crack orientation. The overweight with a counterclockwise orientation is presumably triggered by some overall skewness of fiber orientations.

A further example for local results is given with the development of crack width and crack tractions for a single element. The chosen element is situated in the center of the notch. Fig. 18a shows the development of displacement discontinuity degrees of freedom. The values $\boldsymbol{w}$ computed in the global system, see Eq. (13), are transformed to local values w_n, w_s, see Eqs. (57) and (60). The rotation β is the same in both systems. Crack width w_n initially increases but unloads and reloads in later stages due to internal stress redistributions. Sudden jumps and kinks of crack sliding w_s and rotation β generally result from cracking events in the immediate neighborhood, sign reversals from overall stress redistributions. Corresponding crack tractions are evaluated in two integration points of the A_d-integration of discontinuity forces from Eq. (25). Thus, Fig. 18b basically shows two values for t_n from Eq. (58) and two values for t_s from Eq. (60). Differences in t_n arise from the rotation β. Minor traction oscillations can be seen in the softening part indicating local convergence difficulties from switching between loading and unloading branch of the crack traction - crack width relation, see Fig. 3. This and other detail results require further investigations.

Simulation cracking patterns cannot be directly compared to experimental cracking patterns as the current state of the simulation model is deterministic whereby the experimental specimen behavior is influenced by random material properties. Taking this and other simplifying assumptions into account the simulation model basically seems to be capable to describe FRCC behavior.

4. Conclusions

In the preceding sections a method for modeling reinforced cracked material has been developed with application focuses on fiber reinforced cement composites. Cracking of the cement matrix is modeled with the finite element strong discontinuity approach

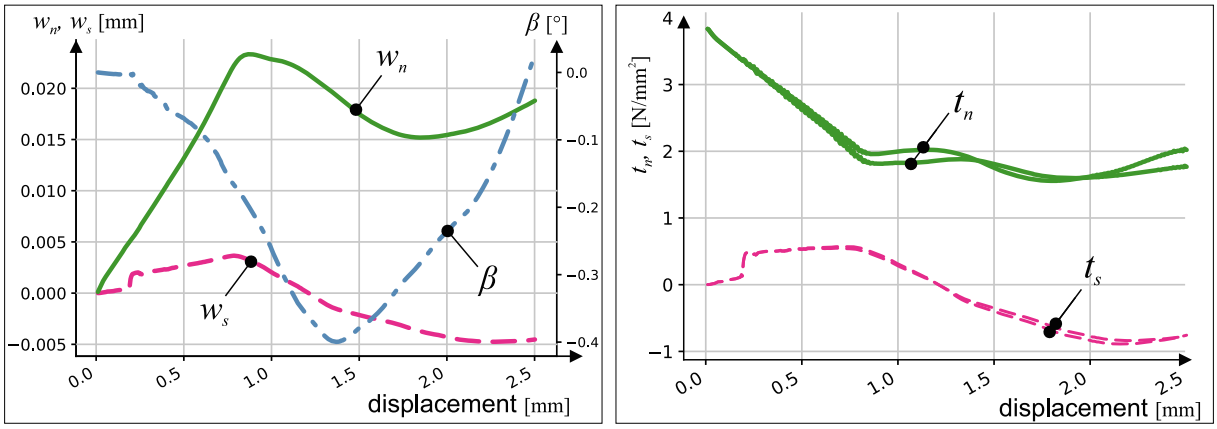


Fig. 18. FRCC simulation single element crack results a) local discontinuity degrees of freedom w_n, w_s, β b) local crack tractions t_n, t_s.

(SDA) whereby crack initiation is ruled by the Rankine criterion depending on the loading history and the fictitious or cohesive crack concept is utilized with crack tractions depending on explicitly computed crack width. First of all, this approach allows for reproduction of the fracture energy independent of element size and naturally solves the mesh dependency problem for softening material behavior. Furthermore, it can be used with nonlinear material laws for the continuum, arbitrary cracking criteria, nonlinear crack traction-crack width relations and multiple cracking with different orientations in a given point.

This is combined with an explicit finite element representation of fibers by finite truss elements assuming no bending stiffness. The dicretization of fibers is independent of the underlying continuum mesh with own truss nodes independent from continuum nodes allowing for an arbitrary fiber position and orientation. Material behavior of fibers may be described as nonlinear. A coupling of truss elements to continuum elements is reached with special bond elements basically acting as spring collections connecting truss nodes and neighbored continuum nodes. This allows for nonlinear bond laws in the longitudinal direction and constrains mutual intersection in the lateral direction by a penalty approach. This type of coupling allows for fibers crossing a discontinuity or crack of the underlying continuum without further arrangements.

The application of methods is demonstrated with, (1) a one-continuum-element setup exposed to different loading types leading to single and multiple cracking, (2) single fiber embedded in a continuum exposed to stretching and pullout, (3) FRCC specimen with a large number of fibers with random position and orientation exposed to tension and an experimental reference available, which altogether basically validate the simulation model. The current approach assumes small displacements, linear elasticity with limited tensile strength for material behaviors before crack initiation or failure, a simple shear retention for cracks, a viscous regularization for stable system behavior and a deterministic view with non scattering system properties.

For further developments and investigations, the extension for large displacements for an improved modeling of fiber pullout is recommended.

In summary, however, it can be stated that a further base is given for target-oriented design of FRCC material composition to reach given objectives of material properties. In addition, the concepts and methods presented allow application not only for short and thin polymer fibers in random position, but also for steel fibers and for structures with long reinforcement in a regular arrangement.

Declaration of Competing Interest

The authors declare that they have no known competing financial interests or personal relationships that could have appeared to influence the work reported in this paper.

Funding

The presented project was funded by the German Research Foundation (DFG) within research training group GRK 2250 *Mineral bonded composites for enhanced structural safety*.

Appendix A. Virtual work principles for SDA

We initially start with the general Hu-Washizu variational principle introducing independent fields for displacements, strains and stresses. A displacement field is assumed as

$$\boldsymbol{u} = \bar{\boldsymbol{u}} + \widehat{\boldsymbol{u}} \tag{A.1}$$

with a part $\bar{\boldsymbol{u}}$ which is continuous over the whole domain under consideration and an enhancement $\widehat{\boldsymbol{u}}$ which, e.g., allows for discontinuities. Strain is assumed as

$$\boldsymbol{\epsilon} = \nabla^{sym}\bar{\boldsymbol{u}} + \widehat{\boldsymbol{\epsilon}} \tag{A.2}$$

with an assumed enhancement $\widehat{\boldsymbol{\epsilon}}$ which is not subject to any interelement continuity requirements. The corresponding four-field Hu-Washizu principle can be written as (Jirásek, 2000)

$$\begin{aligned}
&\int_V \nabla^{sym}\delta\bar{\boldsymbol{u}}^T \cdot \boldsymbol{\sigma}(\boldsymbol{\epsilon})\,\mathrm{d}V = \int_V \delta\bar{\boldsymbol{u}}^T \cdot \boldsymbol{b}\,\mathrm{d}V + \int_{A_t} \delta\bar{\boldsymbol{u}}^T \cdot \boldsymbol{t}\,\mathrm{d}A\\
&\int_V \delta\widehat{\boldsymbol{\epsilon}}^T \cdot [\boldsymbol{\sigma}(\boldsymbol{\epsilon}) - \widehat{\boldsymbol{\sigma}}]\,\mathrm{d}V = 0\\
&\int_V \delta\widehat{\boldsymbol{\sigma}}^T \cdot \left[\nabla^{sym}\widehat{\boldsymbol{u}} - \widehat{\boldsymbol{\epsilon}}\right]\mathrm{d}V = 0\\
&\int_V \nabla^{sym}\delta\widehat{\boldsymbol{u}}^T \cdot \widehat{\boldsymbol{\sigma}}\,\mathrm{d}V = \int_V \delta\widehat{\boldsymbol{u}}^T \cdot \boldsymbol{b}\,\mathrm{d}V + \int_{A_t} \delta\widehat{\boldsymbol{u}}^T \cdot \boldsymbol{t}\,\mathrm{d}A
\end{aligned} \tag{A.3}$$

with variations δ, the symmetric nabla operator ∇^{sym}, assumed stress $\widehat{\boldsymbol{\sigma}}$ and stress $\boldsymbol{\sigma}(\boldsymbol{\epsilon})$ from a material law. With $\widehat{\boldsymbol{u}} = 0, \boldsymbol{u} = \bar{\boldsymbol{u}}$ this corresponds to the basics laid down by (Simo et al., 1990). Finite element interpolations for stresses and strains are assumed with

$$\begin{aligned}
\widehat{\boldsymbol{\sigma}} &= \boldsymbol{S}\cdot\boldsymbol{s}\\
\widehat{\boldsymbol{\epsilon}} &= \boldsymbol{G}\cdot\boldsymbol{e}
\end{aligned} \tag{A.4}$$

Standard interpolation functions $\boldsymbol{N}$ and enhancing functions $\boldsymbol{N}_c$

$$\begin{aligned}
\bar{\boldsymbol{u}} &= \boldsymbol{N}\cdot\boldsymbol{d}\\
\widehat{\boldsymbol{u}} &= \boldsymbol{N}_c\cdot\boldsymbol{d}_c
\end{aligned} \tag{A.5}$$

are used for displacements. Displacement gradients are derived with

$$\begin{aligned}
\nabla^{sym}\bar{\boldsymbol{u}} &= \boldsymbol{B}\cdot\boldsymbol{d}\\
\nabla^{sym}\widehat{\boldsymbol{u}} &= \boldsymbol{B}_c\cdot\boldsymbol{d}_c
\end{aligned} \tag{A.6}$$

Thus, using a Galerkin approach the interpolations yield from Eq. (A.3)

$$\begin{aligned}
&\delta\boldsymbol{d}^T \cdot \int_V \boldsymbol{B}^T\cdot\boldsymbol{\sigma}(\boldsymbol{\epsilon})\,\mathrm{d}V = \delta\boldsymbol{d}^T\cdot\boldsymbol{f}^{ext}\\
&\delta\boldsymbol{e}^T \cdot \left[\int_V \boldsymbol{G}^T\cdot\boldsymbol{\sigma}(\boldsymbol{\epsilon})\,\mathrm{d}V - \int_V \boldsymbol{G}^T\cdot\boldsymbol{S}\,\mathrm{d}V\cdot\boldsymbol{s}\right] = 0\\
&\delta\boldsymbol{s}^T \cdot \left[\int_V \boldsymbol{S}^T\cdot\boldsymbol{B}_c\,\mathrm{d}V\cdot\boldsymbol{d}_c - \int_V \boldsymbol{S}^T\cdot\boldsymbol{G}\,\mathrm{d}V\cdot\boldsymbol{e}\right] = 0\\
&\delta\boldsymbol{d}_c^T \cdot \int_V \boldsymbol{B}_c^T\cdot\boldsymbol{S}\,\mathrm{d}V\cdot\boldsymbol{s} = \delta\boldsymbol{d}_c^T\cdot\boldsymbol{f}_c^{ext}
\end{aligned} \tag{A.7}$$

with

$$\begin{aligned}
\boldsymbol{f}^{ext} &= \int_V \boldsymbol{N}^T\cdot\boldsymbol{b}\,\mathrm{d}V + \int_{A_t}\boldsymbol{N}^T\cdot\boldsymbol{t}\,\mathrm{d}A\\
\boldsymbol{f}_c^{ext} &= \int_V \boldsymbol{N}_c^T\cdot\boldsymbol{b}\,\mathrm{d}V + \int_{A_t}\boldsymbol{N}_c^T\cdot\boldsymbol{t}\,\mathrm{d}A
\end{aligned} \tag{A.8}$$

Different types of enhancement are treated in the following.

1) Displacements are not enhanced, i.e. $\boldsymbol{d}_c = 0, \boldsymbol{u} = \bar{\boldsymbol{u}}$. This makes Eqs. (A.3, A.7)$_4$ obsolete. Eqs. (A.7)$_{1,2}$ reduce to

$$\begin{aligned}
&\int_V \boldsymbol{B}^T\cdot\boldsymbol{\sigma}(\boldsymbol{\epsilon})\,\mathrm{d}V = \boldsymbol{f}^{ext}\\
&\int_V \boldsymbol{G}^T\cdot\boldsymbol{\sigma}(\boldsymbol{\epsilon})\,\mathrm{d}V = 0
\end{aligned} \tag{A.9}$$

The second equation corresponds to the orthogonality condition set by (Simo et al., 1990). Together with a linear elastic material law

$$\boldsymbol{\sigma}(\boldsymbol{\epsilon}) = \boldsymbol{C}\cdot[\nabla^{sym}\bar{\boldsymbol{u}} + \widehat{\boldsymbol{\epsilon}}] = \boldsymbol{C}\cdot[\boldsymbol{B}\cdot\bar{\boldsymbol{u}} + \boldsymbol{G}\cdot\boldsymbol{e}] \tag{A.10}$$

the well-known form

$$\int_v \begin{bmatrix} \boldsymbol{B}^T\cdot\boldsymbol{C}\cdot\boldsymbol{B} & \boldsymbol{B}^T\cdot\boldsymbol{C}\cdot\boldsymbol{G}\\ \boldsymbol{G}^T\cdot\boldsymbol{C}\cdot\boldsymbol{B} & \boldsymbol{G}^T\cdot\boldsymbol{C}\cdot\boldsymbol{G}\end{bmatrix}\mathrm{d}V\cdot\begin{pmatrix}\boldsymbol{d}\\ \boldsymbol{e}\end{pmatrix} = \begin{pmatrix}\boldsymbol{f}^{ext}\\ 0\end{pmatrix} \tag{A.11}$$

is obtained. This is the *statically optimal symmetric formulation* (**SOS**). Regarding kinematic discontinuities SOS ensures natural traction continuity ($\boldsymbol{t} = \boldsymbol{n}\cdot\boldsymbol{\sigma}$) but might introduce spurious stress transfer (Jirásek, 2000).

2) Stresses and strains are not enhanced independently, i.e. $\widehat{\boldsymbol{\sigma}} = \boldsymbol{\sigma}(\boldsymbol{\epsilon}) = \boldsymbol{\sigma}$ and $\boldsymbol{e} = 0$. Strains are derived from enhanced displacements instead

$$\boldsymbol{\epsilon} = \nabla^{sym}\bar{\boldsymbol{u}} + \widehat{\boldsymbol{\epsilon}}, \qquad \widehat{\boldsymbol{\epsilon}} = \nabla^{sym}\widehat{\boldsymbol{u}} \tag{A.12}$$

and we obtain $\widehat{\boldsymbol{\sigma}} - \boldsymbol{\sigma}(\boldsymbol{\epsilon}) = 0$ and $\widehat{\boldsymbol{\epsilon}} - \nabla^{sym}\widehat{\boldsymbol{u}} = 0$ and from Eq. (A.3)

$$\begin{aligned} \int_V \nabla^{sym}\delta\bar{\boldsymbol{u}}^T \cdot \boldsymbol{\sigma}\,\mathrm{d}V &= \int_V \delta\bar{\boldsymbol{u}}^T \cdot \boldsymbol{b}\,\mathrm{d}V + \int_{A_t} \delta\bar{\boldsymbol{u}}^T \cdot \boldsymbol{t}\,\mathrm{d}A \\ \int_V \nabla^{sym}\delta\widehat{\boldsymbol{u}}^T \cdot \boldsymbol{\sigma}\,\mathrm{d}V &= \int_V \delta\widehat{\boldsymbol{u}}^T \cdot \boldsymbol{b}\,\mathrm{d}V + \int_{A_t} \delta\widehat{\boldsymbol{u}}^T \cdot \boldsymbol{t}\,\mathrm{d}A \end{aligned} \tag{A.13}$$

Interpolation of strains according to Eqs. (A.6) yields

$$\boldsymbol{\epsilon} = \boldsymbol{B} \cdot \boldsymbol{d} + \boldsymbol{B}_c \cdot \boldsymbol{d}_c \tag{A.14}$$

and further regarding Eq. (A.13) to

$$\begin{aligned} \delta\boldsymbol{d}^T \cdot \int_V \boldsymbol{B}^T \cdot \boldsymbol{\sigma}\,\mathrm{d}V &= \delta\boldsymbol{d}^T \cdot \boldsymbol{f}^{ext} \\ \delta\boldsymbol{d}_c^T \cdot \int_V \boldsymbol{B}_c^T \cdot \boldsymbol{\sigma}\,\mathrm{d}V &= \delta\boldsymbol{d}_c^T \cdot \boldsymbol{f}_c^{ext} \end{aligned} \tag{A.15}$$

With the linear elastic material law Eq. (A.10) the well known form

$$\int_V \begin{bmatrix} \boldsymbol{B}^T \cdot \boldsymbol{C} \cdot \boldsymbol{B} & \boldsymbol{B}^T \cdot \boldsymbol{C} \cdot \boldsymbol{B}_c \\ \boldsymbol{B}_c^T \cdot \boldsymbol{C} \cdot \boldsymbol{B} & \boldsymbol{B}_c^T \cdot \boldsymbol{C} \cdot \boldsymbol{B}_c \end{bmatrix} \mathrm{d}V \cdot \begin{pmatrix} \boldsymbol{d} \\ \boldsymbol{d}_c \end{pmatrix} = \begin{pmatrix} \boldsymbol{f}^{ext} \\ \boldsymbol{f}_c^{ext} \end{pmatrix} \tag{A.16}$$

is obtained. This is the *kinematically optimal symmetric formulation* (**KOS**). It avoids spurious stress transfer with kinematic discontinuities but might violate natural traction continuity (Jirásek, 2000).

3) The *statically and kinematically optimal nonsymmetric formulation* (**SKON**) avoids the former deficiencies using a Petrov–Galerkin approach. But this leads to unsymmetric systems it is not treated with its details. For its discussion and comparison with SOS and KOS see (Jirásek and Zimmermann, 2001; Gasser et al., 2003).

A variant of KOS will be further discussed in the following. The displacement enhancement is specified as

$$\widehat{\boldsymbol{u}} = H_d \breve{\boldsymbol{u}} = H_d \boldsymbol{N}_c \cdot \boldsymbol{d}_c \tag{A.17}$$

with a continuous field $\breve{\boldsymbol{u}}$ and a Heaviside function H_d defining a line of discontinuity within the domain V. We obtain

$$\begin{aligned} \nabla^{sym}\widehat{\boldsymbol{u}} &= [\delta_d \boldsymbol{n} \otimes \boldsymbol{N}_c + H_d \nabla^{sym}\boldsymbol{N}_c] \cdot \boldsymbol{d}_c \\ &= \boldsymbol{B}_c \cdot \boldsymbol{d}_c \end{aligned} \tag{A.18}$$

with the Dirac-delta function δ_d, the normal $\boldsymbol{n}$ along the line of discontinuity and the tensor product operator $\otimes$ connecting the $\boldsymbol{n}$-index with the first $\boldsymbol{N}_c$-index. Applying the enhancement strain operator $\boldsymbol{B}_c$ to Eq. (A.15)$_2$ yields

$$\begin{aligned} &\delta\boldsymbol{d}_c^T \cdot \int_V \delta_d \left(\boldsymbol{n} \otimes \boldsymbol{N}_c\right)^T \cdot \boldsymbol{\sigma}\,\mathrm{d}V + \delta\boldsymbol{d}_c^T \cdot \int_V H_d \nabla^{sym}\boldsymbol{N}_c^T \cdot \boldsymbol{\sigma}\,\mathrm{d}V \\ &\quad = \delta\boldsymbol{d}_c^T \cdot \boldsymbol{f}_c^{ext} \end{aligned} \tag{A.19}$$

and with the discontinuity traction $\boldsymbol{t} = \boldsymbol{n}^T \cdot \boldsymbol{\sigma}$

$$\delta\boldsymbol{d}_c^T \cdot \int_{A_d} \boldsymbol{N}_c^T \cdot \boldsymbol{t}\,\mathrm{d}V + \delta\boldsymbol{d}_c^T \cdot \int_V H_d \nabla^{sym}\boldsymbol{N}_c^T \cdot \boldsymbol{\sigma}\,\mathrm{d}V = \delta\boldsymbol{d}_c^T \cdot \boldsymbol{f}_c^{ext} \tag{A.20}$$

with the discontinuity surface A_d due to the Dirac-delta integration property. This corresponds to a virtual work principle

$$\begin{aligned} &\int_{A_d} \delta\breve{\boldsymbol{u}}^T \cdot \boldsymbol{t}\,\mathrm{d}V + \int_V H_d \nabla^{sym}\delta\breve{\boldsymbol{u}}^T \cdot \boldsymbol{\sigma}\,\mathrm{d}V \\ &\quad = \int_V H_d\,\delta\breve{\boldsymbol{u}}^T \cdot \boldsymbol{b}\,\mathrm{d}V + \int_{A_t} H_d\,\delta\breve{\boldsymbol{u}}^T \cdot \boldsymbol{t}\,\mathrm{d}A \end{aligned} \tag{A.21}$$

Eqs. (A.21), (A.3)$_1$ are used for weak equilibrium conditions Eqs. (22, 4). The fulfillment of Eqs. (A.21), (A.3)$_1$ should also yield variational consistency regarding the two-field Eqs. (A.13) derived from the four-field Hu-Washizu variational principles Eq. (A.3).

References

Alfaiate, J., Sluys, L.J., 2007. Strong discontinuity formulations: a comparative study. In: Carpinteri, A., Gambarova, P., Ferro, G., & Plizzari, G. (Eds.), Fracture Mechanics of Concrete and Concrete Structures – New Trends in Fracture Mechanics of Concrete. London: Taylor and Francis Group, pp. 147–153..

Alfaiate, J., Simone, A., Sluys, L.J., 2003. Non-homogeneous displacement jumps in strong embedded discontinuities. Int. J. Solids Struct. 40 (21), 5799–5817.

Bathe, K.J., 1996. Finite Element Procedures. Prentice Hall, Englewood Cliffs, New Jersey.

Bažant, Zdeněk P., Lin, Feng Bao, 1988. Nonlocal smeared cracking model for concrete fracture. J. Struct. Eng. 114 (11), 2493–2510.

Bažant, Zdeněk P, Oh, Byung H., 1983. Crack band theory for fracture of concrete. Matériaux et Construction 16 (3), 155–177.

Belytschko, T., Liu, W.K., Moran, B., 2000. Nonlinear Finite Elements for Continua and Structures. John Wiley and Sons, Chichester.

Bentur, Arnon, Mindess, Sidney, 2007. Fibre reinforced cementitious composites. Taylor & Francis.

Bitencourt, A.G., Luís, Manzoli, Osvaldo, L., Bittencourt, Túlio N., Vecchio, Frank J., 2019. Numerical modeling of steel fiber reinforced concrete with a discrete and explicit representation of steel fibers. Int. J. Solids Struct. 159, 171–190.

Bolander, J.E., Saito, S., 1997. Discrete modeling of short-fiber reinforcement in cementitious composites. Adv. Cem. Based Mater. 6 (3), 76–86.

Bouchard, Pierre-Olivier, Bay, François, Chastel, Yvan, Tovena, Isabelle, 2000. Crack propagation modelling using an advanced remeshing technique. Comput. Methods Appl. Mech. Eng. 189 (3), 723–742.

Cunha, V.M.C.F., Barros, J.A.O., Sena-Cruz, J.M., 2011. An integrated approach for modelling the tensile behaviour of steel fibre reinforced self-compacting concrete. Cem. Concr. Res. 41 (1), 64–76.

Cunha, Vítor M.C.F., Barros, Joaquim A.O., Sena-Cruz, José M., 2012. A finite element model with discrete embedded elements for fibre reinforced composites. Comput. Struct. 94–95, 22–33.

Curosu, Iurie, Mechtcherine, Viktor, Millon, Oliver, 2016. Effect of fiber properties and matrix composition on the tensile behavior of strain-hardening cement-based composites (SHCCs) subject to impact loading. Cem. Concr. Res. 82, 23–35.

Curosu, Iurie, Mechtcherine, Viktor, Forni, Daniele, Cadoni, Ezio, 2017. Performance of various strain-hardening cement-based composites (SHCC) subject to uniaxial impact tensile loading. Cem. Concr. Res. 102, 16–28.

Curosu, Iurie, Liebscher, Marco, Mechtcherine, Viktor, Bellmann, Cornelia, Michel, Stefan, 2017. Tensile behavior of high-strength strain-hardening cement-based composites (HS-SHCC) made with high-performance polyethylene, aramid and PBO fibers. Cem. Concr. Res. 98, 71–81.

Dias-da Costa, D., Alfaiate, J., Sluys, L.J., Júlio, E., 2009. A discrete strong discontinuity approach. Eng. Fract. Mech. 76 (9), 1176–1201.

Dvorkin, E.N., Cuitiño, A.M., Gioia, G., 1990. Finite elements with displacement interpolated embedded localization lines insensitive to mesh size and distortions. Int. J. Numer. Methods Eng. 30 (3), 541–564.

Fischer, G., Stang, H., Dick-Nielsen, L., 2007. Initiation and development of cracking in ECC materials: experimental observations and modeling. In: Proceedings of the 6th international conference on fracture mechanics of concrete and concrete structures. S. pp. 1517–1522.

Fries, Thomas-Peter, Belytschko, Ted, 2010. The extended/generalized finite element method: an overview of the method and its applications. Int. J. Numer. Meth. Eng. 84 (3), 253–304.

Gasser, Thomas C, Holzapfel, Gerhard A., 2003. Geometrically non-linear and consistently linearized embedded strong discontinuity models for 3D problems with an application to the dissection analysis of soft biological tissues. Comput. Methods Appl. Mech. Eng. 192 (47–48), 5059–5098.

Gopalaratnam, V.S., Shah, S.P., 1985. Softening response of plain concrete in direct tension. J. Proc. 82, 310–323.

Han, Tong-Seok, Feenstra, Peter, Billington, Sarah, 2003. Simulation of highly ductile fiber-reinforced cement based composite components under cyclic loading. ACI Struct. J. 100, 749–757.

Hartig, Jens, Häußler-Combe, Ulrich, Schicktanz, Kai, 2008. Influence of bond properties on the tensile behaviour of Textile Reinforced Concrete. Cem. Concr. Compos. 30 (10), 898–906.

Hillerborg, Arne, Modéer, Mats, Petersson, P.-E., 1976. Analysis of crack formation and crack growth in concrete by means of fracture mechanics and finite elements. Cem. Concr. Res. 6 (6), 773–781.

Jirásek, M., 1998. Nonlocal models for damage and fracture: comparison of approaches. Int. J. Solids Struct. 35, 4133–4155.

Jirásek, M., 2000. Comparative study on finite elements with embedded discontinuities. Comput. Methods Appl. Mech. Eng. 188 (1–3), 307–330.

Jirásek, Milan, Zimmermann, Thomas, 2001. Embedded crack model: I Basic formulation. Int. J. Numer. Methods Eng. 50 (6), 1269–1290.

Kang, Jingu, Bolander, John E., 2017. Event-based lattice modeling of strain-hardening cementitious composites. Int. J. Fract. 206 (2), 245–261.

Kim, J., 2013. New finite elements with embedded strong discontinuities to model failure of three-dimensional continua (Ph.D. thesis), UC Berkeley..

Kunieda, Minoru, Ogura, Hiroki, Ueda, Naoshi, Nakamura, Hikaru, 2011. Tensile fracture process of Strain Hardening Cementitious Composites by means of three-dimensional meso-scale analysis. Cem. Concr. Compos. 33 (9), 956–965.

Laranjeira, F., 2010. Design-oriented constitutive model for steel fiber reinforced concrete (Ph.D. thesis). Universitat Politècnica de Catalunya.

Laranjeira, F., Molins, C., Aguado, A., 2010. Predicting the pullout response of inclined hooked steel fibers. Cem. Concr. Res. 40 (10), 1471–1487.
Laranjeira, F., Aguado, A., Molins, C., 2010. Predicting the pullout response of inclined straight steel fibers. Mater. Struct. 43 (6), 875–895.
Li, Victor C., 2003. On engineered cementitious composites (ECC). J. Adv. Concr. Technol. 1 (3), 215–230.
Li, Victor C, Leung, Christopher KY., 1992. Steady-state and multiple cracking of short random fiber composites. J. Eng. Mech. 118 (11), 2246–2264.
López, Carlos M, Carol, Ignacio, Aguado, Antonio, 2008. Meso-structural study of concrete fracture using interface elements. I: numerical model and tensile behavior. Mater. Struct. 41 (3), 583–599.
Maalej, M., 2001. Tensile properties of short fiber composites with fiber strength distribution. J. Mater. Sci. 36, 2203–2212.
Moës, Nicolas, Dolbow, John, Belytschko, Ted, 1999. A finite element method for crack growth without remeshing. Int. J. Numer. Methods Eng. 46 (1), 131–150.
Naaman, Antoine E., 2018. Fiber Reinforced Cement and Concrete Composites. Techno Press 3000.
Oliver, J., Huespe, A.E., Samaniego, E., 2003. A study on finite elements for capturing strong discontinuities. Int. J. Numer. Methods Eng. 56 (14), 2135–2161.
Oliver, J., Huespe, A.E., Samaniego, E., Chaves, E.W.V., 2004. Continuum approach to the numerical simulation of material failure in concrete. Int. J. Numer. Anal. Meth. Geomech. 28 (7–8), 609–632.
Padmarajaiah, S.K., Ramaswamy, Ananth, 2002. A finite element assessment of flexural strength of prestressed concrete beams with fiber reinforcement. Cem. Concr. Compos. 24 (2), 229–241.
Pamin, J., de Borst, R., 1999. Gradient enhanced damage and plasticity models for plain and reinforcedconcrete. In: ECCM 99, European Conference on Computational Mechanics, August 31- September 3 1999, Munich, Germany.
Petersson, P-E., 1981. Crack growth and development of fracture zones in plain concrete and similar materials. Lund Institute of Technology, Report TVBM-1006.
Pivonka, P., Ozbolt, J., Lackner, R., Mang, H.A., 2004. Comparative studies of 3D-constitutive models for concrete: applicationtomixedmodefracture. Int. J. Numer. Meth. Eng. 60, 549–570.
Pros, A., Diez, P., Molins, C., 2012. Modeling steel fiber reinforced concrete: numerical immersed boundary approach and a phenomenological mesomodel for concrete-fiber interaction. Int. J. Numer. Meth. Eng. 90 (1), 65–86.
Radtke, F., Simone, A., Sluys, L., 2011. A partition of unity finite element method for simulating non-linear debonding and matrix failure in thin fibre composites. Int. J. Numer. Meth. Eng. 86, 453–476.
Reinhardt, Hans W., Cornelissen, Hans A.W., Hordijk, Dirk A., 1986. Tensile tests and failure analysis of concrete. J. Struct. Eng. 112 (11), 2462–2477.
Ruiz, Gonzalo, 2001. Propagation of a cohesive crack crossing a reinforcement layer. Int. J. Fract. 111 (3), 265–282.
Sancho, J.M., Planas, J., Fathy, A.M., Galvez, J.C., Cendon, D.A., 2007. Three-dimensional simulation of concrete fracture using embedded crack elements without enforcing crack path continuity. Int. J. Numer. Anal. Meth. Geomech. 31 (2), 173–187.
Shehni, Alaleh, Häußler-Combe, Ulrich, Curosu, Iurie, Gong, Ting, & Mechtcherine, Viktor. 2019. Numerical simulation of HS-SHCC under quasi-static tensile loading. 10 th International Conference on Fracture Mechanics of Concrete and Concrete Structures FraMCoS-X, pp. 23–26.
Simo, Juan C, Rifai, M.S., 1990. A class of mixed assumed strain methods and the method of incompatible modes. Int. J. Numer. Methods Eng. 29 (8), 1595–1638.
Smolcic, Z., Ozbolt, J., 2017. Meso scale model for fiber-reinforced-concrete: Microplane based approach. Computers and Concrete 17 (4), 375–385.
Stolarska, M., Chopp, D.L., Moes, N., Belytschko, T., 2001. Modelling crack growth by level sets in the extended finite element method. Int. J. Numer. Meth. Eng. 51, 943–960.
Suwada, Haruhiko, Fukuyama, Hiroshi, 2006. Nonlinear finite element analysis on shear failure of structural elements using high performance fiber reinforced cement composite. J. Adv. Concr. Technol. 4 (1), 45–57.
Švec, Oldřich, Žirgulis, Giedrius, Bolander, John E., Stang, Henrik, 2014. Influence of formwork surface on the orientation of steel fibres within self-compacting concrete and on the mechanical properties of cast structural elements. Cem. Concr. Compos. 50, 60–72.
Willam, Kaspar, Pramono, Eddy, Sture, Stein, 1989. Fundamental Issues of Smeared Crack Models. Shah, Surendra P., Swartz, Stuart E. (Eds.), Fracture of Concrete and Rock. Springer, pp. 142–157..
Zhang, Yiming, Lackner, Roman, Zeiml, Matthias, Mang, Herbert A., 2015. Strong discontinuity embedded approach with standard SOS formulation: element formulation, energy-based crack-tracking strategy, and validations. Comput. Methods Appl. Mech. Eng. 287, 335–366.